Establishment of an African green monkey model for COVID-19 and protection against re-infection

Courtney Woolsey [1,2], Viktoriya Borisevich[1,2], Abhishek N. Prasad [1,2], Krystle N. Agans[1,2], Daniel J. Deer[1,2], Natalie S. Dobias[1,2], John C. Heymann[3], Stephanie L. Foster[1,2], Corri B. Levine [1,2], Liana Medina[1,2], Kevin Melody [1,2], Joan B. Geisbert[1,2], Karla A. Fenton[1,2], Thomas W. Geisbert [1,2] ✉ and Robert W. Cross [1,2]

Severe acute respiratory syndrome coronavirus 2 (SARS-CoV-2) is responsible for an unprecedented global pandemic of COVID-19. Animal models are urgently needed to study the pathogenesis of COVID-19 and to screen vaccines and treatments. We show that African green monkeys (AGMs) support robust SARS-CoV-2 replication and develop pronounced respiratory disease, which may more accurately reflect human COVID-19 cases than other nonhuman primate species. SARS-CoV-2 was detected in mucosal samples, including rectal swabs, as late as 15 days after exposure. Marked inflammation and coagulopathy in blood and tissues were prominent features. Transcriptome analysis demonstrated stimulation of interferon and interleukin-6 pathways in bronchoalveolar lavage samples and repression of natural killer cell- and T cell–associated transcripts in peripheral blood. Despite a slight waning in antibody titers after primary challenge, enhanced antibody and cellular responses contributed to rapid clearance after re-challenge with an identical strain. These data support the utility of AGM for studying COVID-19 pathogenesis and testing medical countermeasures.

Severe acute respiratory syndrome coronavirus 2 (SARS-CoV-2), the etiological agent of coronavirus disease 2019 (COVID-19), emerged in Wuhan, China in late 2019 and rapidly swept the globe. As of 12 October 2020, over 37 million confirmed cases and 1 million deaths have been reported worldwide[1]. No licensed vaccines or therapeutics currently exist, although many clinical trials are underway. While clinical testing is ultimately needed to assess drug safety and efficacy, bypassing preclinical evaluation warrants caution due to the potential for disease enhancement[2–4]. A careful assessment in animal models could reveal possible immune complications elicited by vaccines and therapies before their release to the public. Moreover, animal models are critical to understanding aspects of pathogenesis and immunity that are not easily addressed or feasible in humans.

Several animal species including rodents, ferrets and nonhuman primates (NHPs) were found to support SARS-CoV-2 replication and displayed mostly subclinical to mild illness after challenge[5–11]. Syrian hamsters developed mild to moderate disease and pulmonary lesions that resolved within 2 weeks[6,12]. While each of these models has utility in the study of COVID-19, NHPs have the closest physiological resemblance to humans. This feature allows an accurate comparison of host responses to infection and enhances the predictive efficacy of medical countermeasures. Recently, studies evaluating the pathogenic potential of SARS-CoV-2 in cynomolgus and rhesus macaques were reported. Limited viral replication was observed in both models; rhesus macaques developed mild pneumonia and few clinical signs, whereas disease in cynomolgus macaques was less pronounced[8,10,11,13]. These results suggest that certain NHP species may serve as better models than others for coronavirus infections. For SARS-CoV, AGMs were found to support the highest level of viral replication followed by cynomolgus macaques and rhesus macaques when all three species were

challenged in parallel[14]. Only AGMs challenged with SARS-CoV had marked replication in the lower respiratory tract in association with viral pneumonia, consistent with human SARS. As SARS-CoV and SARS-CoV-2 share high genomic similarity and the same putative host receptor, angiotensin-converting enzyme 2 (refs. [15,16]), we reasoned that AGMs might serve as a useful model for COVID-19.

Here, we exposed AGMs to low-passage SARS-CoV-2 and evaluated their potential as a model for COVID-19. We demonstrate that AGMs mimic several aspects of human disease, including pronounced viral replication and pulmonary lesions, using a greater than twofold lower dose of SARS-CoV-2 than has been employed in many rhesus and cynomolgus macaque studies. Transcriptomic analyses of bronchoalveolar lavage (BAL) and peripheral blood samples revealed that AGMs exhibit similar immune profiles as humans[17,18]. Moreover, our data show that AGMs are protected from re-infection after re-challenge at 35 days after exposure. Thus, the AGM model can be used to analyze the host immune response, conduct pathogenesis studies and screen potential vaccines and therapeutics against COVID-19.

Results

Clinical disease in AGMs. In a narrowly focused study to examine acute pathogenesis and protection from back-challenge, we exposed six adult AGMs to 4.6×10^5 plaque-forming units (p.f.u.) of SARS-CoV-2 by combined intratracheal and intranasal routes. A cohort of three animals was euthanized at 5 d post-infection (dpi), while the remaining three animals were re-challenged via the same routes at 35 dpi (identical virus strain and dose). These group numbers are in line with previous SARS-CoV-2 NHP studies[8–11,13,19,20]. Back-challenged subjects were monitored for an additional 22 d. For each cohort, longitudinal blood and bronchoalveolar lavage (BAL)

[1]Department of Microbiology and Immunology, University of Texas Medical Branch, Galveston, TX, USA. [2]Galveston National Laboratory, University of Texas Medical Branch, Galveston, TX, USA. [3]Department of Radiology, University of Texas Medical Branch, Galveston, TX, USA. ✉e-mail: twgeisbe@utmb.edu

Table 1 | Clinical findings of AGMs infected with SARS-CoV-2

Subject no.	Sex	Clinical illness	Clinical pathology
AGM-1	F	Fever (d3), decreased appetite (d4, 5). Subject survived to study end point (d5).	Monocytosis (d5); neutrophilia (d4); eosinophilia (d4); basophilia (d4); > sixfold ↑ CRP (d4); > onefold ↑ CRP (d5)
AGM-2	F	Decreased appetite (d1–5). Subject survived to study end point (d5).	Lymphocytopenia (d2–5); monocytopenia (d2, 3, 5); eosinopenia (d4); basopenia (d3, 4) thrombocytopenia (d4); >onefold ↑ in ALT (d3, 4); >onefold ↑ in GGT (d3–5); onefold ↑ in CRP (d3, 4)
AGM-3	M	Fever (d3). Subject survived to study end point (d5).	Lymphocytopenia (d5); thrombocytopenia (d4); monocytosis (d4); neutrophilia (d4); eosinophilia (d4); onefold ↑ in CRE (d4); >fourfold ↑ in CRP (d4), hypercapnia (d3, 5)
AGM-4	F	Fever (d4); decreased appetite (d1–10, 12, 13, 15–17, 20–24, 27, 29, 30, 33, 34, **36/1–39/4**, **42/7–44/9**), anorexia (**d41/6**). Subject survived to study end point (**d57/22**).	Lymphocytopenia (d2, 3); neutropenia (d2, 3, 5), thrombocytopenia (d2); neutrophilia (d4, 15); eosinophilia (d4, 7, 12, 15); monocytopenia (d21); eosinopenia (d2, 3, **38/3**, **42/7**); basopenia (d2, 3, **38/3**, **40/5**, **42/7**); hypoglycemia (d7, 9, 12); >sixfold ↑ CRP (d4); >twofold ↑ CRP (d5), hypercapnia (d7, **40/5**, **42/7**)
AGM-5	M	Decreased appetite (d8,10, 17, 22–24, 34, **36/1–39/4**,). Subject survived to study end point (**d57/22**).	Monocytopenia (2, 4, 9, 21, 28, **38/3**, **49/14**); neutropenia (d2, 28, **57/22**); eosinopenia (d2, 3, 21, 28, 33, **40/5**, **49/14**); basopenia (d2–5, 7, 9, 21, 28, 33, **49/14**); thrombocytopenia (d33); >twofold ↑ CRP (d4), **hypoglycemia (d57/22)**, hypercapnia (d7, 15, 28, **38/3**)
AGM-6	F	Decreased appetite (d1–3, 5–10, 13–17, 22–24, **36/1**); nasal exudate (d40). Subject survived to study end point (**d57/22**).	Lymphocytopenia (d7, **57/22**); monocytosis (d12); eosinopenia (d2–5, 12, 21, 33); basopenia (2–5, 7, 9, 12, 15, 21, 28, 33); basophilia (**d49/14**); >onefold ↑ in CRP (d4), hypercapnia (d7, 12, **35/0**, **40/5**, **42/7**, **57/22**)

Days after SARS-CoV-2 challenge are in parentheses. Clinical findings following back-challenge (d35/0) are in bold, with the day following primary challenge listed first and the day following back-challenge listed second. All reported findings are in comparison to baseline (d0 for primary challenge, d35/0 for back-challenge) values. Decreased appetite is defined as some food but not all food consumed from the previous day. Anorexia is defined as no food consumed from the previous day. Lymphocytopenia, monocytopenia, neutropenia, eosinopenia, basopenia and thrombocytopenia are defined by a ≥35% drop in numbers of lymphocytes, monocytes, neutrophils, eosinophils, basophils and platelets, respectively. Monocytosis, neutrophilia, eosinophilia and basophilia are defined by a twofold or greater increase in numbers of monocytes, neutrophils, eosinophils or basophils, respectively. Hypoglycemia is defined by a ≥25% decrease in concentrations of glucose. Hypercapnia was defined as having a partial CO_2 > 4 mm Hg over d0 baseline values.

samples were collected throughout the study up until the respective study end point.

After primary challenge, AGMs experienced mild and varied clinical signs of disease. In five of six animals, monkeys exhibited decreased appetite compared to baseline (0 dpi) and a brief period of elevated body temperature suggestive of fever in three of six animals at 3–4 dpi (Table 1 and Extended Data Fig. 1). A biphasic increase in partial CO_2 pressures, indicative of hypercapnia, was noted in four of six animals following primary and back-challenge, but no overt changes in partial O_2 pressures were noted. Transient lymphocytopenia and thrombocytopenia were observed in all AGMs, most prominently at 2–7 dpi. Markers for renal (creatinine (CRE) and blood urea nitrogen) and hepatic function (alanine aminotransferase (ALT), aspartate aminotransferase, γ-glutamyl transferase (GGT), alkaline phosphatase) remained mostly unchanged (less than twofold increases); however, C-reactive protein (CRP), a marker of acute systemic inflammation, increased two to sevenfold in all animals 2–5 dpi (Table 1). No systemic increases in CRP were observed following back-challenge.

Viral loads. Viral loads in blood, mucosal swabs and BAL fluid were quantified following primary and secondary exposure by quantitative PCR with reverse transcription (RT–qPCR) (Fig. 1a,c,e,g) and plaque titration (Fig. 1b,d,f,h). Following primary challenge, all subjects had detectable quantities of viral RNA (vRNA) and infectious virus in nasal secretions at 2 dpi, with infectious viral titers ranging from ~2–4 log p.f.u. ml⁻¹ (Fig. 1a,b). Nasal shedding of vRNA occurred up to 9 dpi in AGM-4 and 12 dpi in AGM-5. Following secondary exposure to SARS-CoV-2, vRNA was detected in nasal swabs of AGM-4 at 38 dpi and AGM-5 at 38 and 40 dpi (3 and 5 d after re-challenge). Both vRNA and infectious virus were detected in oral swabs of three animals (AGM-2, AGM-5, AGM-6) 3 dpi, and persisted in AGM-5 up to 7 dpi (Fig. 1c,d). Infectious virus was only detected in the rectal swab of a single animal (AGM-3) 3–5 dpi;

however, vRNA was detected in AGM-4 and AGM-5 rectal samples 12 and 15 dpi, respectively (Fig. 1e,f). Both vRNA and infectious virus was present in BAL fluid of all subjects 3–7 dpi (Fig. 1g,h). Neither vRNA nor infectious virus was detected in whole blood or plasma, respectively, indicating a lack of circulating cell-associated or free virus in the peripheral blood (data not shown). No infectious virus was evident in nasal samples after secondary exposure nor was vRNA or infectious virus found in mucosal swabs or BAL fluid, (Fig. 1b–h), suggesting that AGMs were protected from re-infection following SARS-CoV-2 back-challenge.

Tissues collected at necropsy from AGMs euthanized at day 5 dpi or 57/22 dpi were also examined for viral loads. For the cohort euthanized at 5 dpi, vRNA and infectious virus abundance was highest in tissues from the upper and lower respiratory tracts (Extended Data Fig. 2a,b). Substantial quantities of vRNA in some or all animals were detected in major organs, including lymphoid tissue (~10^4–10^6 genome equivalents (GEq) per g tissue), the heart (~10^5 GEq per g tissue), the digestive tract (~10^3–10^7 GEq per g tissue) and immunologically privileged sites such as the central nervous system, eyes and urogenital tract (~10^4–10^6 GEq per g tissue). For the re-challenged cohort, AGM-4 had detectable vRNA (~10^3–10^7 GEq g⁻¹ tissue) in inguinal and mesenteric lymph node, spleen, heart and ileocecal junction tissues; AGM-5 had detectable vRNA (~10^5–10^6 GEq per g tissue) in liver, brain stem, ileum, ileocecal junction, eye, conjunctiva and reproductive tissue; and AGM-6 had detectable vRNA (~10^6 GEq per g tissue) in duodenal tissue. However, considerable reductions of vRNA in specific tissues of the back-challenged cohort were noted, particularly in the upper and lower respiratory tracts. While infectious titers were prominent in the lungs of subjects euthanized at 5 dpi, no infectious virus was found in the lungs, or any other collected tissues, of re-challenged animals. Our data indicate that SARS-CoV-2 replicates abundantly in the respiratory tract of AGMs, but that viral loads are reduced in re-challenged subjects.
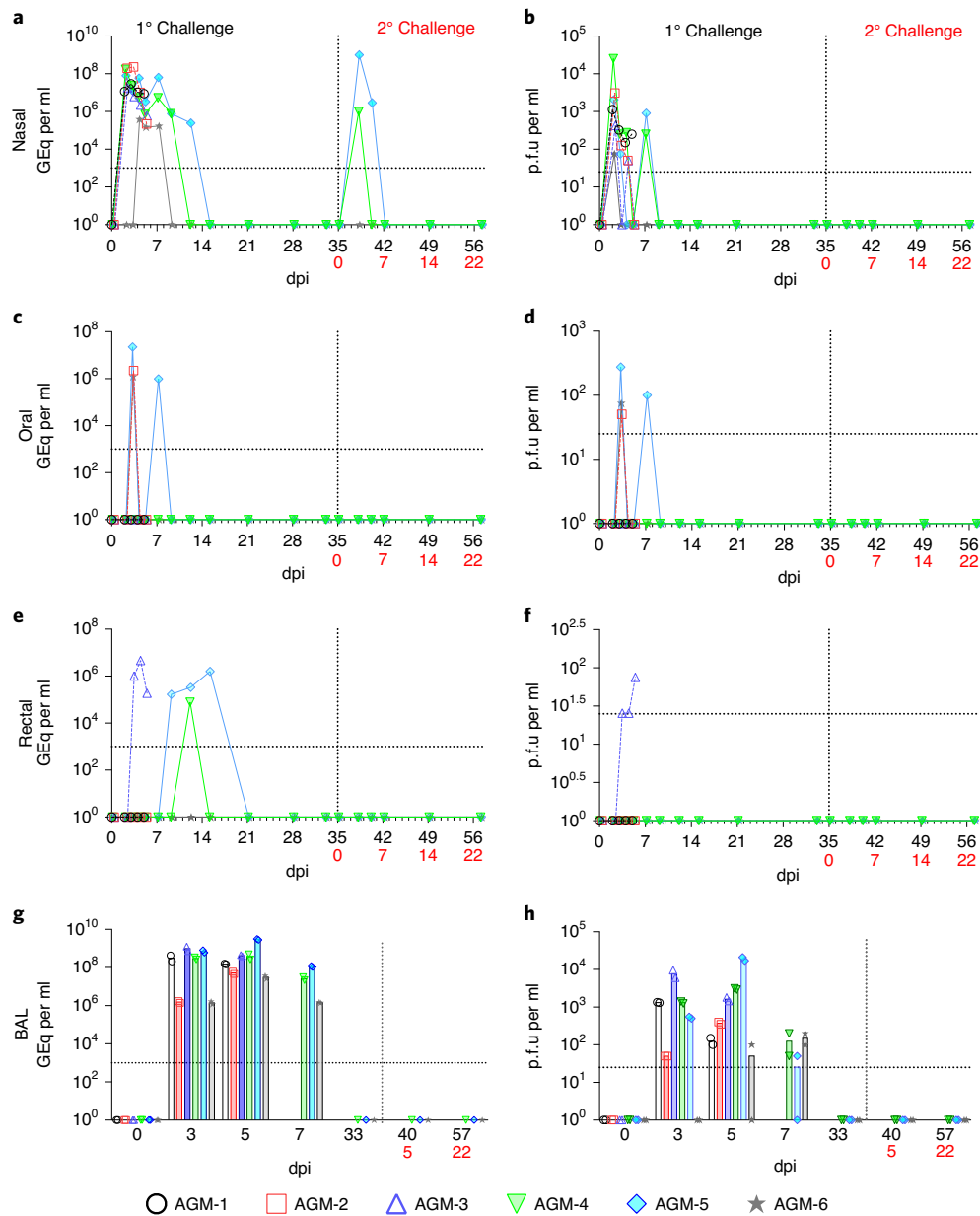
Fig. 1 | Detection of SARS-CoV-2 vRNA and infectious virus in mucosal swabs and BAL fluid. a–h, Nasal swabs (**a,b**), oral swabs (**c,d**), rectal swabs (**e,f**), and BAL fluid (**g,h**) from AGMs infected with SARS-CoV-2 were subjected to RT–qPCR (**a,c,e,g**) or plaque titration (**b,d,f,h**). For all graphs, dashed lines and open symbols (AGM-1, AGM-2, AGM-3) indicate AGMs euthanized 5 dpi (*n* = 3); solid lines (AGM-4, AGM-5, AGM-6) indicate AGMs held to 57 dpi or 22 d after re-challenge (*n* = 3). Data plotted are each duplicate RT–qPCR reaction or well per subject/sample in a single experiment. Red text indicates the day of back-challenge.

Gross and histological findings. Necropsy revealed varying degrees of pulmonary consolidation with hyperemia and hemorrhage in the lungs. (Fig. 2a–f). The lung from a historical SARS-CoV-2-negative AGM was included for comparison that was not subjected to BAL procedures (Fig. 2g). AGMs at 5 dpi had marked to severe locally extensive pulmonary lesions (Fig. 2a–c), whereas AGMs at 22 d after back-challenge had mild to moderate locally extensive pulmonary lesions (Fig. 2d–f). In all AGMs, the most severe lesions were located in dorsal aspects of the lower lung lobes. A board-certified veterinary pathologist approximated lesion severity for each lung lobe. Average lung severity scores were reduced in back-challenged AGMs versus animals euthanized at 5 dpi (two-tailed Student's *t*-test; *P* = 0.02; Supplementary Table 1). Thoracic radiographs taken on −1, 2, 3, 4 and 5 dpi were inconclusive (Extended Data Fig. 3).

Histologically, all three AGMs euthanized at 5 dpi developed varying degrees of multifocal pulmonary lesions suggestive of inflammatory processes directly associated with the congestion and hemorrhage noted on gross examination. In the most severely affected animal (AGM-3), histologic features of acute bronchointerstitial pneumonia (Fig. 3a) included neutrophilic inflammation concentrated at terminal bronchioles in association with macrophages, numerous multinucleated giant cells and syncytial cells that were positive by immunohistochemistry (IHC) for cytokeratin (an epithelial cell marker) (Fig. 4b). Continuous with the terminal bronchiolitis was evidence of focal alveolar damage with scant hyaline membrane formation (Fig. 4e), type II pneumocyte hyperplasia and flooding of alveolar spaces with pulmonary edema, hemorrhage and fibrin (Fig. 3c). Rarely, exuberant reparative lesions
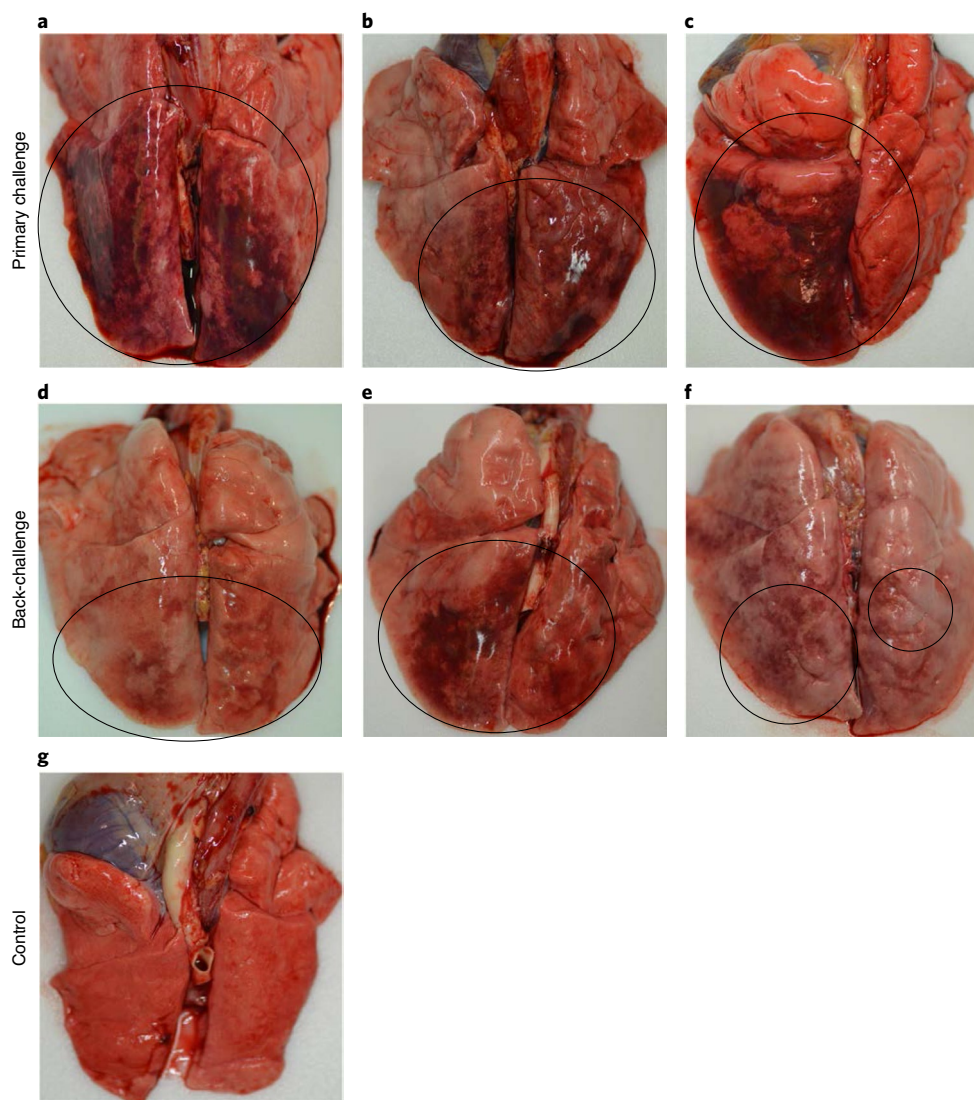
Fig. 2 | Pulmonary gross changes in AGMs infected with SARS-CoV-2. a–c, Dorsal view of lungs from AGM-1 (**a**), AGM-2 (**b**) and AGM-3 (**c**) subjects euthanized at 5 dpi exhibited marked locally extensive pulmonary consolidation with hyperemia and hemorrhage (circled regions). **d–f**, Dorsal view of lungs from AGM-4 (**d**), AGM-5 (**e**) and AGM-6 (**f**) subjects euthanized at 57 dpi (22 d after re-challenge) exhibited mild locally extensive pulmonary consolidation with hyperemia and hemorrhage (circled regions). **g**, Dorsal view of a normal lung with no notable lesions from a SARS-CoV-2-negative AGM.

of collagenous tissue proliferations were noted protruding within the terminal airways reminiscent of early bronchiolitis obliterans organizing pneumonia (BOOP)-like lesions (Fig. 4d)[21]. Interstitial pneumonia was prominent in the lesser-affected regions of the lung, along with congestion, increased numbers of alveolar macrophages and microthrombi within alveolar capillaries (Fig. 3d,f). Modest amounts of immature loose collagen also diffusely expanded alveolar septae were observed and are highlighted with trichrome stain (Fig. 4h). Ulcerative tracheobronchitis was present and characterized by multifocal extensive epithelial erosion associated with hemorrhage, fibrin accumulation and infiltrating mixed inflammatory cells.

In the lesser-affected monkeys (AGM-1 and AGM-2), pulmonary lesions lacked acute erosive inflammation within the trachea and bronchi; however, interstitial pneumonia with rare multinucleated giant cells, lymphocytic perivascular cuffs and mild lymphocytic tracheobronchitis were present. Co-localization of SARS-CoV-2 antigen with pulmonary lesions presented as positive immunohistochemical labeling within the cytoplasm of respiratory epithelium of the bronchus, alveolar macrophages and type I and

type II pneumocytes (Figs. 3b,e and 4c). Genomic SARS-CoV-2 RNA was detected by in situ hybridization in pneumocytes and was associated with alveolar macrophages within acute inflammation centered on terminal bronchioles (Fig. 4a). Although, we did not observe overwhelming damage to pneumocytes from SARS-CoV-2 infection lacking inflammatory infiltrates in the primary tissues at the time of necropsy, it would be premature for us to wholly rule out that the virus as benign. There is likely a combination of events in which the virus, host inflammatory response and host reparative/healing response are responsible for lesions noted early and late in the disease course.

Accordingly, polymerized fibrin was abundant and present within bronchial lumen associated with the acute inflammation at sites of epithelial erosion, flooding alveolar spaces associated with alveolar damage, within inflamed alveolar walls associated with microthrombi (Fig. 3c,f) and rarely along the pleural surface. Fibrin was prominent within large and small caliber vessels throughout the representative section of lung, but was not associated with any obvious adherent thrombus. Additional findings included positive IHC for SARS-CoV-2 antigen in rare mononuclear cells within
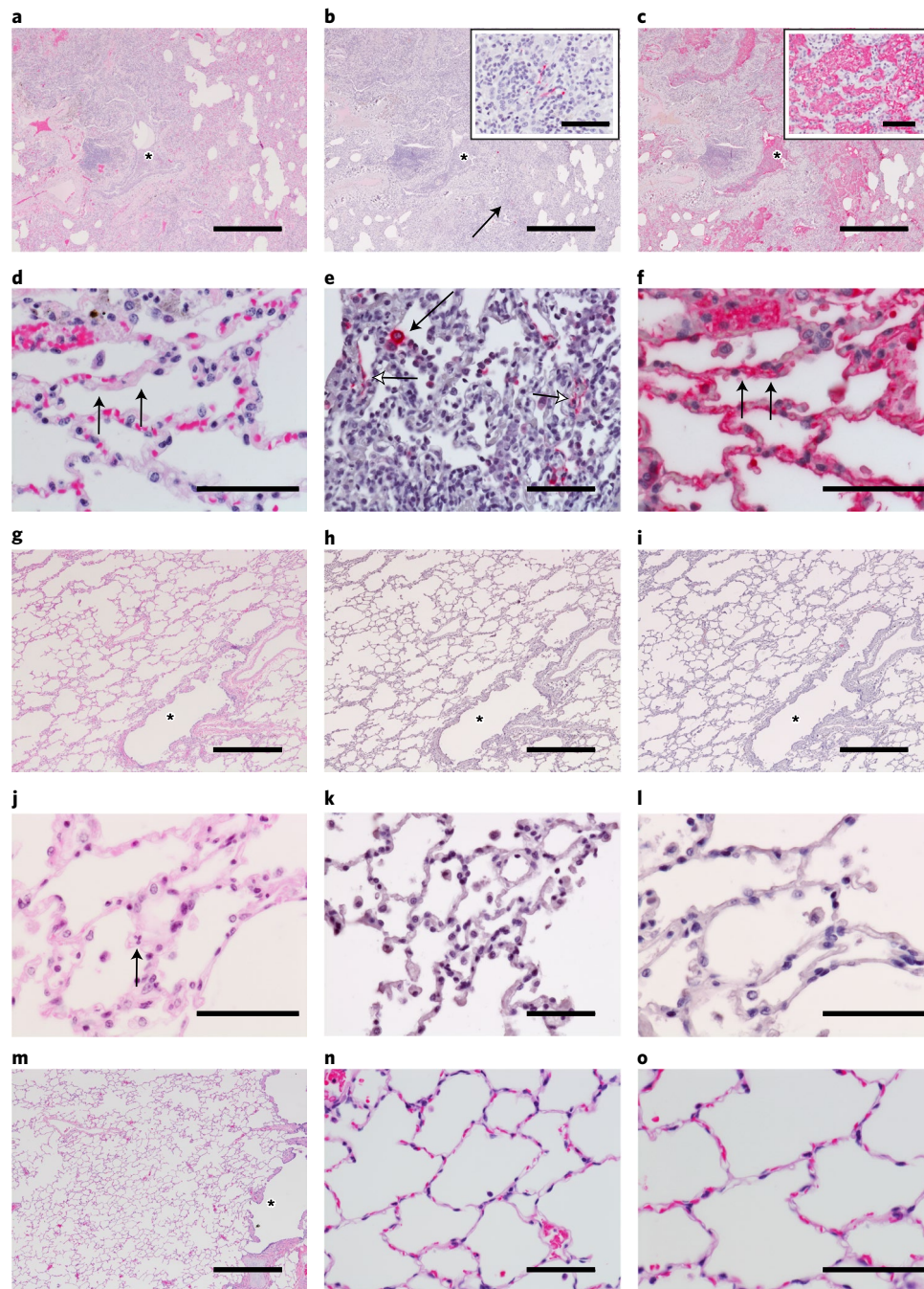
Fig. 3 | Pulmonary histologic changes in AGMs infected with SARS-CoV-2. a–c, Low magnification of serial sections of the left lower lung lobe of AGM-3. Locally extensive, marked, acute bronchiolitis (*) and interstitial pneumonia (**a**). SARS-CoV-2 IHC-positive pneumocytes (arrow indicating the ×60 inset) colocalized with bronchiolitis (*) (**b**). Flooded alveolar sacs with fibrin (inset at ×40) that colocalized with acute bronchiolitis (*) (**c**). **d–f,** Higher magnification of lung alveoli images of representative AGMs 5 dpi with SARS-CoV-2. **d,** Interstitial pneumonia with fibrin microthrombi within alveolar capillaries (arrows). **e,** SARS-CoV-2-positive labeling of type I (white arrow) and type II (black arrow) pneumocytes. **f,** Serial section of tissue with positive fibrin labeling within alveolar capillaries (arrows). **g–i,** Low magnification of serial sections of the right lower lung lobe of AGM-6 with mild interstitial pneumonia and patent bronchioles (*) (**g**), no immunolabeling for anti-SARS-CoV-2 antigen (**h**) and no immunolabeling for anti-fibrin antigen (**i**). **j–l,** Higher magnification of lung alveoli images of AGM-4 mild interstitial pneumonia with neutrophil indicated (arrow) (**j**), no immunolabeling for anti-SARS-CoV-2 antigen (**k**) and no immunolabeling for anti-fibrin antigen (**l**). **m–o,** SARS-CoV-2-negative control AGM lung at low magnification with patent bronchioles (*) and high magnification (**m**) and with no substantial lesions (**n,o**). H&E staining (**a,d,g,j,m–o**), IHC labeling for anti-SARS-CoV-2 antigen (red) (**b,e,h,k**) and IHC labeling for anti-fibrin antigen (red) (**c,f,i,l**). Images captured at ×4 (**a–c,g–i,m**), ×40 (**e,k,n**) and ×60 (**d,f,j,l,o**) magnification. Scale bars, 500 μm (**a–c,g–i,m**) and 50 μm (**b** inset, **c** inset, **d–f,j–l, n,o**).

the Peyer's patches of the duodenum (Fig. 4f) and associated with granulomatous foci within the renal interstitium (Fig. 4n). All other major organs were unremarkable.

To ascertain whether re-challenged AGMs were protected from pulmonary damage, we next performed histological staining and IHC on tissues from this cohort. Twenty-two days after

back-challenge, lesions indicative of previous infection with SARS-CoV-2 were evidenced as moderate interstitial pneumonia with lymphohistiocytic inflammation, congestion, increased numbers of alveolar macrophages and rarely focal alveolar smooth muscle hypertrophy (Figs. 3g,j and 4i). Chronic ulcerative tracheobronchitis was rarely present and characterized by focal ulcerated respiratory epithelium with associated fibrin and inflammation. Multifocally, immature loose collagen diffusely expanded alveolar septae were present and are highlighted with trichrome stain (Fig. 4i). No notable immunolabeling for fibrin was detected in the alveoli of the examined lung sections (Fig. 3i,l) and no immunolabeling for SARS-CoV-2 antigen was observed in the lung (Fig. 3h,k) or any other examined organ.

In the liver, mild chronic inflammation and intravascular organizing fibrin was noted and characterized by mild sinusoidal leukocytosis, random lymphocytic infiltrates, congestion and organizing intravascular fibrin. In the kidney, all three subjects had lymphocytic interstitial nephritis and two of three monkeys (AGM-5, AGM-6) had evidence of chronic bilateral glomerulonephritis with hyalinization of some glomeruli, fibrin accumulation within glomerular tufts, glomerular tuft atrophy with dilation of Bowman's capsule and periglomerular fibrosis (Fig. 4l). Marked regions of interstitial lymphohistiocytic inflammation associated with fibrosis and contracture of the renal cortex were prominent. Thus, lung, liver and kidney tissue of re-challenged AGM seem to exhibit chronic reparative changes.

Humoral and cellular responses. Assessment of humoral responses in AGMs revealed five of six animals seroconverted, including all three animals held past 5 dpi, with the earliest detection of anti-SARS-CoV-2 IgG or neutralizing titers (50% plaque reduction values) occurring at 5 dpi (Fig. 5a). Total virus-specific IgG titers peaked at 15–21 dpi (1:200–1:6,400) in the back-challenged group and were followed by a period of slightly waning antibody titers in two of three animals that were amplified 1–3 weeks after re-challenge (1:12,800–1:25,600) (Fig. 5a). Notably, IgG titers directed at the nucleoprotein, full-length spike (S1 + S2 ectodomain) and receptor-binding domain (RBD) appeared later than total IgG and followed a similar trend of waxing and waning (Fig. 5b–d). RBD-specific IgA in all three remaining monkeys was not detected until 12 dpi and remained relatively low (1:200–1:800) until 1–2

weeks after back-challenge, wherein titers increased to 1:1,1600–1:6,400 (Fig. 5e). Notably, the appearance of RBD-specific IgG corresponded with neutralizing titers at 5 (AGM-1, AGM-3) and 7 (AGM-4) dpi, emphasizing the importance of the RBD domain in antibody-mediated virus neutralization (Fig. 5c,f). Neutralizing titers ranged from 1:8–1:32 after primary challenge and peaked at 1:512–1:1,024 after back-challenge (Fig. 5f). Strong anamnestic immune responses, coupled with the presence of vRNA in tissues and nasal swabs after secondary exposure to SARS-CoV-2, indicated a lack of sterilizing immunity. Similarly, cellular responses detected by ELISPOT (interferon (IFN)-γ^+ interleukin (IL)-2$^-$ and IFN-γ^+IL-2$^+$ cells) of peripheral blood mononuclear cells (PBMCs) to SARS-CoV-2 peptide pools increased over the course of the study relative to pre-challenge baselines (0 dpi) and were augmented upon re-challenge (Fig. 5g). By 21 dpi, mean spike-specific cellular responses were higher than nucleoprotein-specific responses, similar to human cases[22]. Unsurprisingly, IFN-γ^-IL-2$^+$ cells were not detected as they are understood to be rare in circulation[23]. Together, these results suggest that antibody and cellular responses slightly wane after primary challenge, but are enhanced after re-challenge to potentially protect animals from re-infection.

BAL and blood transcriptome analyses. To unravel the AGM host immune response to SARS-CoV-2 infection, we temporally tracked transcriptional changes in blood and BAL samples during the acute phase of disease. For this analysis, blood and BAL RNA samples were assayed in parallel at 3 ($n = 6$), 5 ($n = 6$) and 7 ($n = 3$) dpi to discriminate between localized and systemic immune responses to infection; additionally, we analyzed blood samples at an early (2 dpi; $n = 6$) and convalescent time point (21 dpi; $n = 3$).

Examination of normalized sample populations by principal-component analysis revealed time-dependent expression changes in BAL and blood samples with minimal dimensional separation between 3 and 5 dpi samples (Extended Data Fig. 4a,b). Blood 2 dpi samples mostly clustered with 3 and 5 dpi samples, whereas blood 7 dpi samples mostly clustered with pre-challenge and convalescent (21 dpi) samples.

SARS-CoV-2-specific targets (envelope, membrane, nucleocapsid, orf1ab, orf3a, orf7a, orf8 and surface glycoprotein) were also quantified in BAL samples. Copious reads of SARS-CoV-2-specific

Fig. 4 | Additional histologic changes in AGMs infected with SARS-CoV-2. a–f, Pulmonary lesions in representative AGMs 5 dpi (**a–e**) and IHC (**f**) of the duodenum. Genomic SARS-CoV-2 RNA (red) detected by in situ hybridization in mononuclear cells near a multinucleated giant cell associated with acute bronchiolitis, ×60 magnification (**a**). Syncytial cells (arrows) within a terminal bronchiole, ×60 magnification and inset with a pan-cytokeratin IHC-positive syncytial cell indicating epithelial origin (arrow) within a terminal bronchiole, ×60 (**b**). SARS-CoV-2-positive IHC labeling (red) associated with acute bronchiolitis, ×20 magnification, and in the inset, SARS-CoV-2 IHC-positive respiratory epithelium of the bronchus, ×40 magnification (**c**). Terminal bronchioles with multiple luminal protrusions of loose collagen covered by respiratory epithelium that is reminiscent of early formation of bronchiolitis obliterans organizing pneumonia (BOOP)-like lesions (*), ×20 magnification, and inset, serial section of tissue stained with trichrome highlighting immature collagen (*) (blue), ×20 magnification (**d**). Loss of alveolar architecture, marked expansion of septa and formation of faint hyaline membranes (arrow), ×20 magnification, and inset, IHC-positive pan-cytokeratin (brown) of hyaline membranes from serial section of tissue (arrow), ×20 magnification (**e**). IHC SARS-CoV-2-positive (red) mononuclear cell within the Peyer's patches of the duodenum (arrow), ×20 magnification (**f**). **g,** Trichrome stain of AGM alveolar septate basement membrane (blue) from a SARS-CoV-2-naive AGM, ×40 magnification. **h,i,** Trichrome stain of alveolar septate with collagenous expansion (blue) from a SARS-CoV-2 AGM 5 dpi, ×40 magnification (**h**) and AGM 57 dpi and focal smooth muscle hyperplasia (arrows), ×40 magnification (**i**). **j–o,** Comparison of kidneys from naive AGMs, AGMs 5 dpi and 57 dpi SARS-CoV-2. Renal congestion with no substantial lesions in naive SARS-CoV-2 AGM, ×10 magnification, and higher magnification in the inset of glomerulus with trichrome stain with no prominent findings, ×40 (**j**). Renal congestion with no notable findings in AGM 5 dpi, ×10 magnification, and higher magnification in the inset of glomerulus with trichrome stain with mild glomerular fibrosis, ×40 (**k**). Marked renal interstitial lymphocytic inflammation (*) with glomerulopathy and expanded Bowman's space (white arrow) in AGM 57 dpi, ×10 magnification, and higher magnification in the inset of glomerulus with glomerular fibrosis (blue) and marked periglomerular fibrosis (black arrow), ×40 (**l**). Fibrin IHC-negative AGM kidney ×10 maginification, and higher magnification of fibrin-negative glomerulus, ×40 (**m**). IHC SARS-CoV-2-positive (red) mononuclear cell (arrow) within renal interstitium of AGM 5 dpi, ×60 magnification (**n**). Fibrin IHC-positive (red) multifocal within glomerular capillaries and renal interstitium of AGM 57 dpi, ×10 magnification, and high magnification of fibrin-positive glomerulus, ×40 (**o**). H&E staining (**b,d,e,j–l**), IHC labeling for anti-SARS-CoV-2 antigen (red) (**c, c** inset, **f,n**), IHC labeling for anti-fibrin antigen (red) (**m, m** inset, **o, o** inset), IHC labeling for anti-pan-cytokeratin (brown) (**b** inset and **e** inset), SARS-CoV-2 in situ hybridization (**a**), trichrome (**d** inset, **g–i, j** inset, **k** inset, **l** inset). Images captured at ×10 (**j–m,o**), ×20 (**c,d, d** inset, **e, e** inset, f), ×40 (**c** inset, **g–i, j** inset, **k** inset, l inset, **m** inset, **o** inset) and ×60 magnification (**a,b, b** inset, **n**). Scale bars, 100 μm (**c,d, d** inset, **e, e** inset, **f,j–m,o**) 50 μm (**a,b, b** inset, **c** inset, **g–i, j** inset, **k** inset, **l** inset, **n, o** inset).

probes were detected in BAL samples at 3 and 5 dpi, but no significant abundance in any particular gene product was recognized at any time point (Extended Data Fig. 4c).

Analysis of global changes revealed upregulated differentially expressed (DE) RNAs shared between BAL and blood samples were involved in IFN signaling (*MX1*, *MX2*, *IFIT1*, *IFIT3* and *IFI44*), RIG-I/MDA-5 pattern recognition (*DDX58* and *IFIH1*) and RNaseL signaling (*OAS1*, *OAS2*, *OAS3* and *OASL*) (Fig. 6a–f). Robust IFN signaling was observed in the blood as early as 2 dpi (Extended Data Fig. 5a,b). In contrast, shared repressed DE transcripts were implicated in major histocompatibility complex class II-based antigen presentation (*HLA-DQA1* and *HLA-DQB1*) (Fig. 6a–c,f).

In BAL samples, expression of leukocyte immunoglobulin-like receptor B5 (*LILRB5*) was consistently decreased at 3, 5 and 7 dpi

(Fig. 6a,c,e). Additional downregulated BAL DE messenger RNAs at 5 and 7 dpi are involved in lipid antigen presentation (*CD1D*), the complement system (*C1QA*, *C1QB*), calgranulin-mediated calcium sensing (*S100A8*, *S100A9*) or major histocompatibility complex class II antigen presentation (*HLA-DPB1*, *HLA-DRB1*, *HLA-DRA*). Increased expression of *IL8* and *CCR5* transcripts were measured in BAL samples at 7 dpi pointing to inflammation in the lung mediated by macrophages and/or neutrophil populations.

In the blood, upregulated immune signatures at 5 dpi suggested plasma cell differentiation (*XBP1*) and lymphocyte activation (*CD38*), as well as immune tolerance/T cell exhaustion (*CD274* (PD-1), *IDO1*). Repressed transcripts at 3 or 5 dpi pointed to a reduction in mitogen-activated protein kinase signaling (*MAP4K1*), natural killer (NK) cells (*KLRK1*, *KLRF1*, *KLRG1*), T cells (*CD3D*,
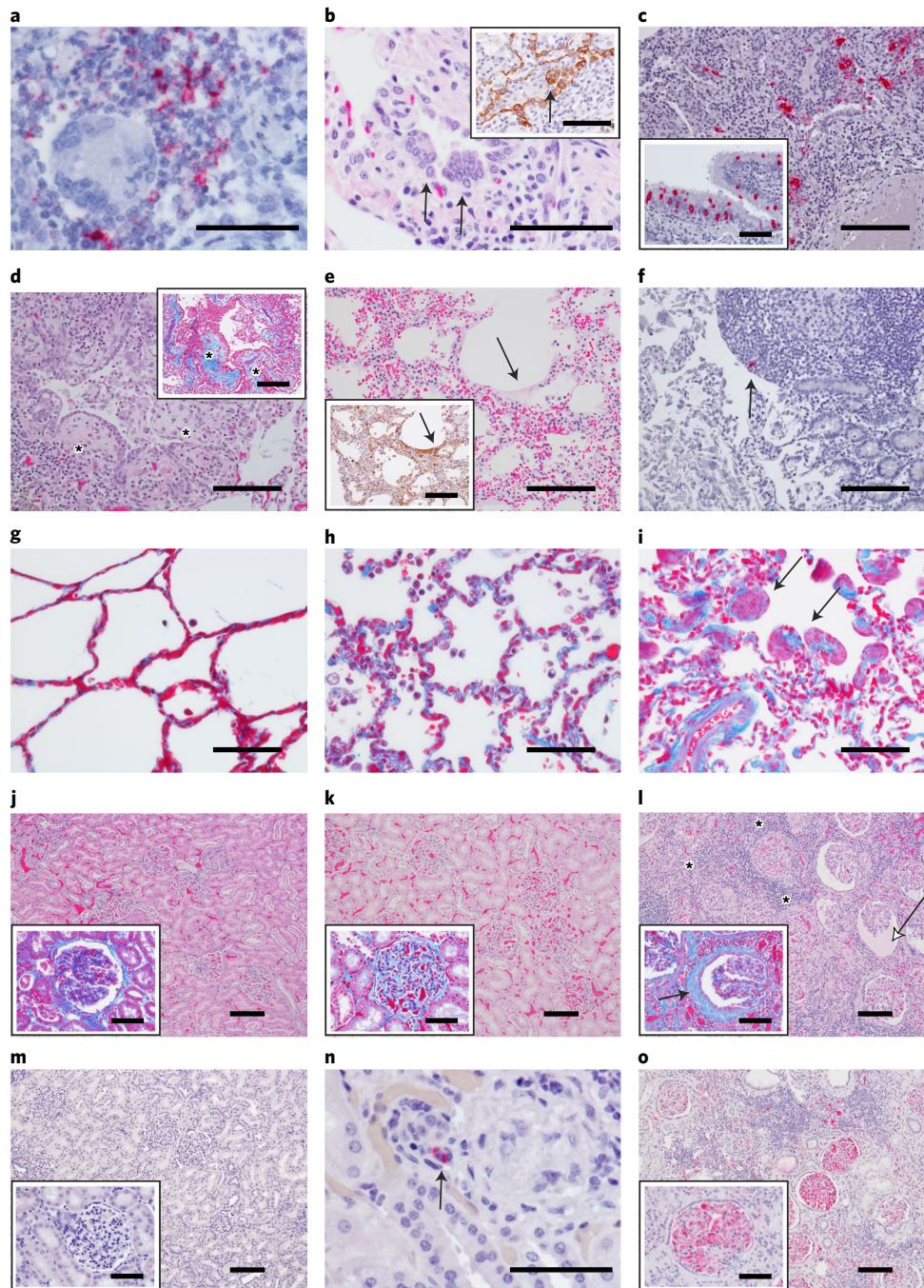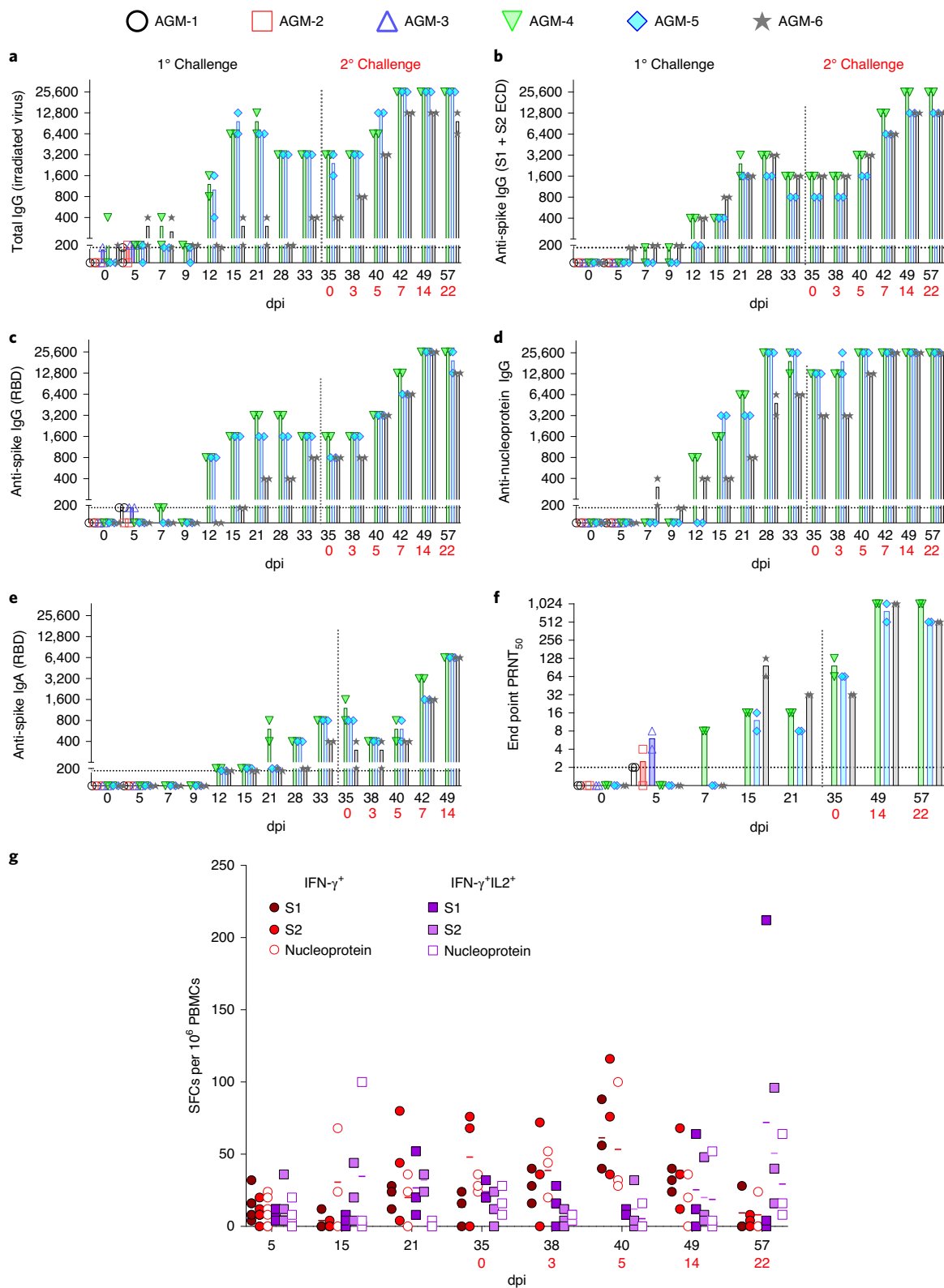
Fig. 5 | Humoral and cellular responses in SARS-CoV-2-infected AGMs. a–e, Anti-SARS-CoV-2 IgG binding titers. RBD, receptor binding domain of SARS-CoV-2 spike; S1, S1 subunit of the SARS-CoV-2 spike (contains RBD); S2, S2 subunit of the SARS-CoV-2 spike, ECD, extracellular domain of the SARS-CoV-2 spike protein (contains both S1 and S2 subunits). **f**, Neutralizing titers in AGM serum. $PRNT_{50}$ values indicate 50% neutralization compared to virus control plates. All plaque counts were calculated from duplicate wells at each dilution. **g**, PBMCs were stimulated with $1\,\mu g\,ml^{-1}$ of peptide pools spanning the SARS-CoV-2 nucleoprotein or spike (split into two pools). Unstimulated cells and PBMCs stimulated with pokeweed mitogen (PWM) served as negative and positive controls, respectively (data not shown). The spike pools contained 158 or 157 15mer peptides with 11 amino acid overlaps, and the N pool contained 13mer peptides with 10 amino acid overlaps. Reported values were calculated by subtracting the number of spot forming cells (SFCs) in a given unstimulated sample from its respective stimulated counterpart at the corresponding dpi. Values were subtracted from a pre-challenge baseline (0 dpi). Data plotted are each duplicate reciprocal dilution titer per subject in a single experiment. Red text indicates the day of back-challenge.
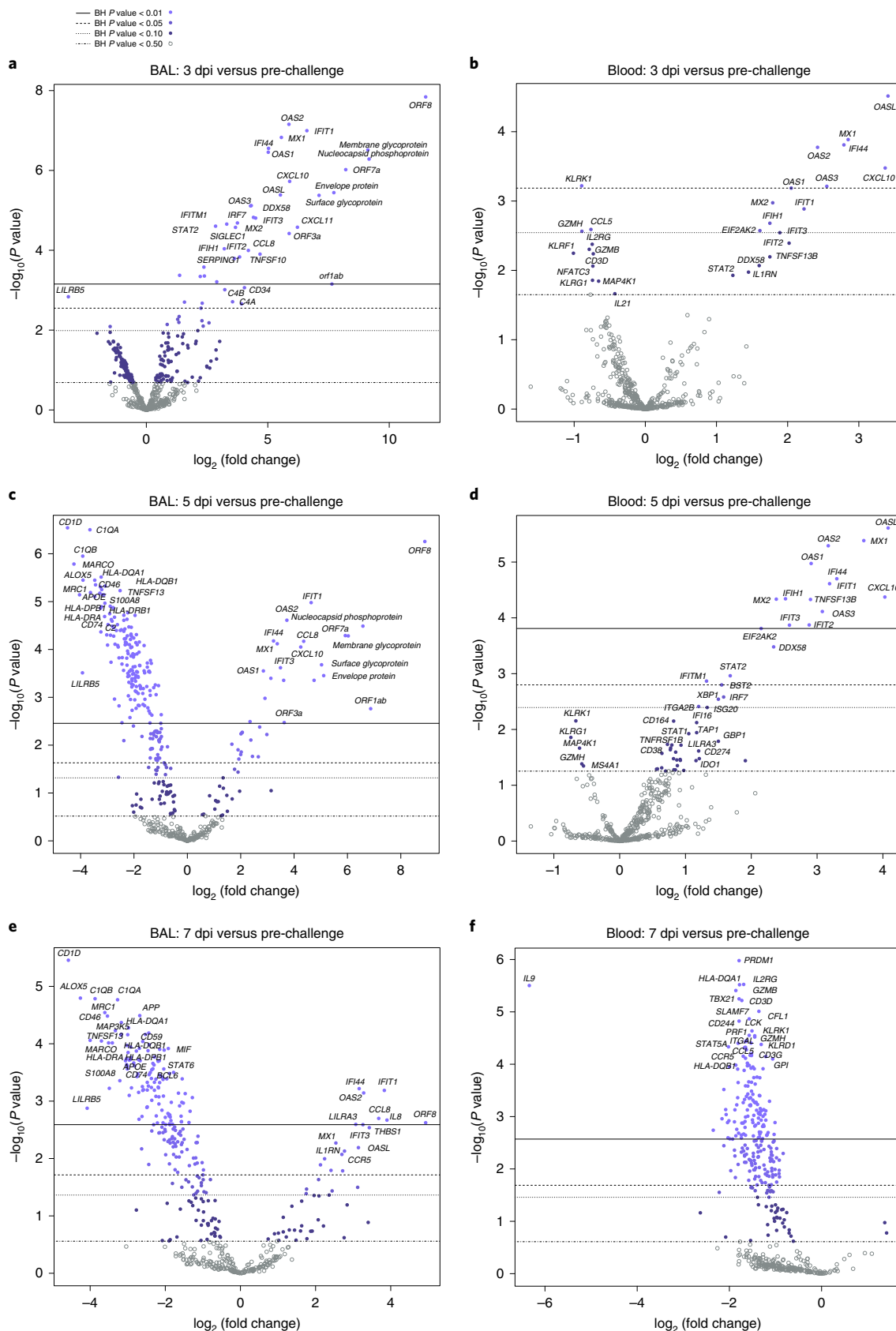
Fig. 6 | Volcano plots indicating transcriptional changes in BAL and blood samples at selected time points. a–f, RNA expression changes were evaluated in BAL (**a,c,e**) and blood samples (**b,d,f**) from SARS-CoV-2-infected AGMs at 3, 5 and 7 dpi. Displayed are the mean $-\log_{10}$ (P values) and $\log_2$ fold changes for each mRNA target from $n = 6$ biological replicates in a single experiment for 3 and 5 dpi time points (**a–d**) and $n = 3$ biological replicates for the 7 dpi time point (**e,f**) relative to a pre-challenge baseline (-8 dpi). Horizontal lines within each plot indicate adjusted P value thresholds. Targets highlighted in blue indicate false discovery rate (FDR)-adjusted P values <0.10. A Benjamini–Hochberg test was employed to derive FDR-adjusted P values.

IL2RG), NK and T cell cytotoxicity (*GZMH*, *GZMB*, *GZMK*, *IL21*) and type 1 helper T cells (*TBX21*) (Fig. 6b,d). The majority of DE mRNAs were downregulated in BAL and blood samples at 7 dpi (Fig. 6e,f), as well as the convalescent stage (Extended Data Fig. 5a–c). These data potentially reflect the onset of disease resolution in the lung and peripheral blood compartments at 7 dpi. This observation is consistent with a reduction in viral titers and SARS-CoV-2-specific gene transcripts in BAL samples at this time point.

Functional enrichment of DE transcripts was next used to decipher signaling networks associated with infection in the lungs and blood. For this analysis, each BAL or blood dataset was filtered by dpi (3, 5, 7). At all time points, other than the 7 dpi blood group, positive z scores correlated with induction of canonical pathways related to stimulation of immunity and clearance of viral infections (Fig. 7a). Although a slight reduction in positive z scores in BAL samples at 7 dpi was detected, these pathways were significantly downregulated (negative z scores) in the blood at 7 dpi, again indicating rapid resolution of the acute phase of disease in the blood compartment. At 3 and 5 dpi, upstream regulators and causal networks predicted induction of IFN, tumor necrosis factor and Toll-like receptor signaling, which was resolved at 7 dpi in the blood. Causal networks associated with negative regulation of innate immunity (*CACTIN*) and ubiquitination (*UBE3C*, *RNF216*) were consistently downregulated in both BAL and blood samples at 3 and 5 dpi. To compare BAL and blood responses early in infection, we mapped JAK/STAT signaling pathways for each dataset. Unlike BAL samples, evidence of negative regulation of type I IFN mediated by downregulation of IFNAR2 signaling was evident in blood as early as 3 dpi (Fig. 7b). At 5 dpi, network maps depicting the relatedness of prominent gene clusters indicated sustained activation of innate immunity in BAL samples with evidence of regulation of cytokine production. In contrast, blood networks were predominantly involved in adaptive immunity or regulation of innate immunity (Fig. 7c). At 7 dpi, predicted activation of IFN-α was noted in the BAL dataset, whereas predicted inhibition of IFN-α was strongly apparent in the blood dataset (Fig. 7d). Collectively, these results suggest clearance of virus in the blood and lungs at 7 dpi with rapid resolution of immune responses in the blood.

Systemic cytokine and fibrinogen concentrations. Serum concentrations of pro-inflammatory IL-6, IL-8, monocyte chemoattractant protein, IP-10, IL-12 and immunoregulatory IL-10 largely peaked at 2 dpi for most animals corresponding to subsequent recruitment of monocytes and neutrophils in the blood (Extended Data Fig. 6a–f and Table 1). Although IFN-related transcripts were highly expressed in blood and BAL samples (Fig. 6a–f), animals only secreted modest amounts of IFN-β (Extended Data Fig. 6g). As IL-6 is a main regulator of acute-phase fibrinogen synthesis and elevated fibrinogen and other coagulation abnormalities are thought to correlate with disease severity in hospitalized patients[24,25], we also measured the abundance of this clotting factor. Circulating fibrinogen concentrations surged in four of six monkeys at 4 dpi, indicating potential coagulation abnormalities in these animals (Extended Data Fig. 6h). This observed coagulopathy aligns with our gross

pathology findings of substantial hemorrhage in the lung of monkeys euthanized at 5 dpi.

Discussion

AGMs serve as disease models for several respiratory pathogens[14,26–29]. Guided by previous data suggesting that AGMs were a superior model for SARS-CoV in terms of exemplifying human viral replication kinetics and histopathological features[14], we investigated their suitability as a model for SARS-CoV-2 infection. In our study, we show AGMs develop mild, moderate or severe pulmonary lesions following SARS-CoV-2 infection. AGMs challenged with SARS-CoV-2 did not develop debilitating clinical illness; however, these animals exhibited an impressive array of disease features observed in humans. A low fraction of NHPs may develop severe disease similar to humans infected with SARS-CoV-2. The heterogeneous responses of AGMs are a chief attribute that makes them an attractive model compared to inbred, more genetically homogenous, rodent models. Furthermore, NHPs have the closest physiological resemblance to humans allowing an accurate comparison of host responses to infection and enhancing the predictive efficacy of medical countermeasures.

Other NHP species, including rhesus and cynomolgus macaques, were evaluated as animal models for COVID-19, with rhesus macaques more closely exhibiting human symptoms[9–11,30]. Data on these NHP models are difficult to interpret, as many early studies used high challenge doses. The limited viral replication reported in these studies may also represent artifacts at the challenge and sampling site. Moreover, data from these studies do not reflect the high viral replication and/or shedding kinetics observed in humans[10,11,19]. A recent study evaluating the effect of various challenge doses in rhesus macaques down to 10^4 total p.f.u. per animal was the first model to demonstrate clear evidence of replication in nasal swabs by viral subgenomic mRNA content. However, no demonstration of infectious virus was reported in respiratory tissues of these animals. Subgenomic mRNA content did not seem to be challenge-dose-dependent nor was there evidence of clinical disease observed in humans (fever, weight loss, respiratory distress). However, immune responses to viral challenge were apparent[13]. Given the lack of infectious virus in the lower respiratory tract and only mild disease presentation, others have suggested that the rhesus macaque model may be more appropriate for studying vaccination or therapeutic responses against SARS-CoV-2 rather than modeling human COVID-19 (ref. [31]).

We demonstrate that AGMs recapitulate human infection and recovery and rapidly cleared infection after re-challenge. Transient lymphopenia and thrombocytopenia and elevated serum markers associated with systemic inflammation were evident. Fever is estimated in ~78% of human patients presenting with COVID-19 (ref. [32]). Using surgically implanted temperature data loggers, elevated body temperature was detected in three animals at 3–4 dpi, indicative of mild transient fever. To date, only one study reported elevated core temperatures in SARS-CoV-2-infected NHPs immediately following challenge[10]. The rapid induction of fever in this study clouds interpretation as to whether an acute response to

---

Fig. 7 | Functional enrichment of DE mRNAs in SARS-CoV-2-infected AGM BAL and blood samples. All data were normalized against a pre-challenge baseline (−8 dpi) for each time point and sample type. A higher degree of transparency denotes values that are less extreme in the dataset. Unless otherwise noted, red indicates an increased measurement and green indicates a decreased measurement. **a**, Heat map depicting the most highly upregulated and downregulated canonical pathways, upstream regulators and causal networks in BAL and blood samples at each time point; red indicates high expression (*z* scores), blue indicates low expression, white indicates similar expression, and gray indicates insufficient transcripts mapping to the indicated pathway. IRF, interferon regulatory factor; NF, nuclear factor; PRR, pattern recognition receptor; SLE, systemic lupus erythematosus; T$_H$17, type 17 helper T cell; TNF, tumor necrosis factor. **b**, Jak/STAT signaling pathways illustrating differential responses in BAL and blood datasets at 3 dpi. **c**, Network maps depicting gene networks associated with SARS-CoV-2 infection in each dataset. T$_H$1, type 1 helper T cell; T$_H$2, type 2 helper T cell. **d**, Differential regulation of IFN-α in BAL and blood samples at 7 dpi; orange lines indicate predicted activation, blue lines indicate predicted inhibition, yellow lines indicate findings inconsistent with the state of the downstream molecule, and gray lines indicate an effect is not predicted.
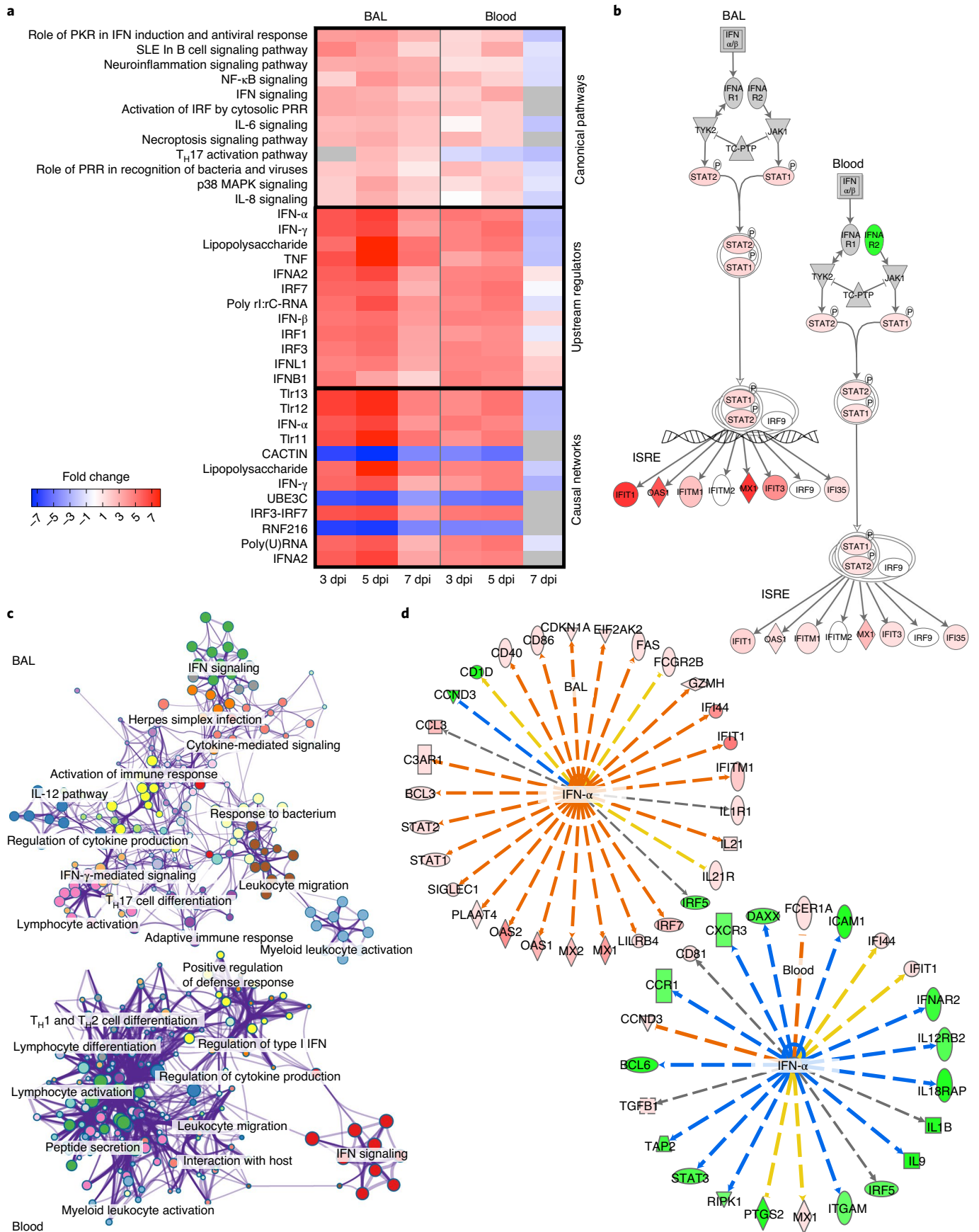
inoculum or a bona fide response to viral replication was reported. Transient fever may be a feature of disease in other NHP models of COVID-19, but perhaps not consistently observed, as only infrequent periodic monitoring is common.

A notable aspect of the AGM model for SARS-CoV-2 infection is the development of pronounced viral pneumonia. All AGMs in this study exhibited pulmonary consolidation with hemorrhage, varying in severity between animals and lung lobes. Histology and IHC of lung tissue revealed multifocal lesions of varying severity with co-localization of viral antigen, confirming that infection with SARS-CoV-2 resulted in marked viral pneumonia in these animals. Notably, numerous histological features of the lungs from AGMs infected with SARS-CoV-2 mirrored those reported in human COVID-19 cases[33–35]. A caveat to this study is that we did not directly compare vRNA, gross pathology and histological changes at 57 d after primary challenge with a group that was not re-exposed. Therefore, it is unclear whether changes in the back-challenged AGMs were as a result of primary challenge or back-challenge. Nevertheless, average lesion severity scores were lower in back-challenged AGMs and no notable immunolabeling for fibrin or SARS-CoV-2 antigen was observed in the lung or any other examined organ in these subjects.

We performed thoracic radiographs on all six SARS-CoV-2-infected AGMs. It is our opinion that radiographs from our study, while consistent with reports in SARS-CoV-2-infected macaques[8,10,30], belie the degree of lesions and hemorrhage of the lungs seen at necropsy and do not convincingly demonstrate SARS-CoV-2-induced disease. Specifically, opacities and changes observed in radiographs are nonspecific and could be due to atelectasis, inadequate inspiratory effort (unable to control inspiratory effort in NHPs) or BAL collection procedures, among other etiologies. Important to this discussion, the US Centers for Disease Control does not recommend either radiography or computed tomography as a primary screening tool nor does the American College of Radiology due to poor specificity and sensitivity[36]. A study of 636 ambulatory patients with COVID-19 did not detect chest radiograph abnormalities in 60% of confirmed cases[37]. Furthermore, a multidisciplinary panel comprised principally of radiologists and pulmonologists with experience of managing patients with COVID-19 recommended against chest radiography in cases with mild clinical features[38].

Our data show that infection of AGMs with SARS-CoV-2 results in upregulation of IFN-stimulated genes and IL-6 and IL-8 signaling in the lungs and peripheral blood; in the blood, NK- and T cell-associated transcripts were repressed, which is consistent with human cases[17,18,39,40]. Functional enrichment of DE mRNAs pointed to rapid viral clearance with tightly controlled responses in the blood. Our results indicate evaluation of lung and blood samples is important to fully capture the state of disease, as some key differences were observed between these compartments particularly in terms of gene regulation. We observed increased serum concentrations of these ILs as well as other pro-inflammatory cytokines and chemokines elevated in human cases. Additionally, we detected a rise in circulating fibrinogen in a majority of AGMs, which is implicated in thrombosis and vascular injury in human patients[24,25].

The potential for re-infection in humans with SARS-CoV-2 is speculated, but the risk factors or incidence are unknown. This possibility is concerning as antibody titers to endemic human coronaviruses (for example, HCoV-229E) are reported to gradually wane and re-infection with homologous virus has been reported[41,42]. Others have demonstrated protection against back-challenge of rhesus macaques[13,19]. Similarly, we describe the capacity of AGM challenged with SARS-CoV-2 to achieve natural immunity. Notably, all animals held past 5 dpi seroconverted and, despite relatively low neutralizing titers at back-challenge, rapidly cleared the secondary challenge inoculum. Immunity was not sterilizing as vRNA was detected in nasal swabs shortly after infection, yet infectious

virus was not detected, suggesting the risk for infectiousness post-exposure may be present, albeit low. Nonetheless, anamnestic humoral and cellular responses were uniformly demonstrated in all back-challenged animals. Interestingly, the development of circulating anti-spike RBD binding IgG and IgA coincided with an increase in neutralizing sera potency. Future studies examining antibody type and potency from the mucosa may further inform compartmentalization of protective antibodies.

Our comprehensive evaluation indicates that AGMs can be used to study pathogenesis and the host response to SARS-CoV-2 infection. Notably, this model may prove valuable in streamlining the most promising medical countermeasures for human use.

Online content

Any methods, additional references, Nature Research reporting summaries, source data, extended data, supplementary information, acknowledgements, peer review information; details of author contributions and competing interests; and statements of data and code availability are available at https://doi.org/10.1038/s41590-020-00835-8.

References

1. World Health Organization. *Coronavirus Disease (COVID-19) Situation Report* https://www.who.int/docs/default-source/coronaviruse/situation-reports/20201012-weekly-epi-update-9.pdf (2020).
2. Tseng, C. T. et al. Immunization with SARS coronavirus vaccines leads to pulmonary immunopathology on challenge with the SARS virus. *PLoS ONE* **7**, e35421 (2012).
3. Bolles, M. et al. A double-inactivated severe acute respiratory syndrome coronavirus vaccine provides incomplete protection in mice and induces increased eosinophilic proinflammatory pulmonary response upon challenge. *J. Virol.* **85**, 12201–12215 (2011).
4. Weingartl, H. et al. Immunization with modified vaccinia virus Ankara-based recombinant vaccine against severe acute respiratory syndrome is associated with enhanced hepatitis in ferrets. *J. Virol.* **78**, 12672–12676 (2004).
5. Bao, L. et al. The pathogenicity of SARS-CoV-2 in hACE2 transgenic mice. *Nature* https://doi.org/10.1038/s41586-020-2312-y (2020).
6. Chan, J. F. W. et al. Simulation of the clinical and pathological manifestations of coronavirus disease 2019 (COVID-19) in golden Syrian hamster model: implications for disease pathogenesis and transmissibility. *Clin. Infect. Dis.* https://doi.org/10.1093/cid/ciaa325 (2020).
7. Kim, Y. I. L. et al. Infection and rapid transmission of SARS-CoV-2 in ferrets. *Cell Host Microbe* **27**, 704–709 (2020).
8. Rockx, B. et al. Comparative pathogenesis of COVID-19, MERS, and SARS in a nonhuman primate model. *Science* **368**, 1012–1015 (2020).
9. Yu, P. et al. Age-related rhesus macaque models of COVID-19. *Anim. Model. Exp. Med.* **3**, 93–97 (2020).
10. Munster, V. J. et al. Respiratory disease in rhesus macaques inoculated with SARS-CoV-2. *Nature* **585**, 268–272 (2020).
11. Shan, C. et al. Infection with novel coronavirus (SARS-CoV-2) causes pneumonia in rhesus macaques. *Cell Res.* **30**, 670–677 (2020).
12. Imai, M. et al. Syrian hamsters as a small animal model for SARS-CoV-2 infection and countermeasure development. *Proc. Natl Acad. Sci. USA* **117**, 16587–16595 (2020).
13. Chandrashekar, A. et al. SARS-CoV-2 infection protects against rechallenge in rhesus macaques. *Science* **369**, 812–817 (2020).
14. McAuliffe, J. et al. Replication of SARS coronavirus administered into the respiratory tract of African green, rhesus and cynomolgus monkeys. *Virology* **330**, 8–15 (2004).
15. Letko, M., Marzi, A. & Munster, V. Functional assessment of cell entry and receptor usage for SARS-CoV-2 and other lineage B betacoronaviruses. *Nat. Microbiol.* **5**, 562–569 (2020).
16. Shang, J. et al. Cell entry mechanisms of SARS-CoV-2. *Proc. Natl Acad. Sci. USA* https://doi.org/10.1073/pnas.2003138117 (2020).
17. Zhou, Z. et al. Heightened innate immune responses in the respiratory tract of COVID-19 patients. *Cell Host Microbe* **27**, 883–890 (2020).
18. Wen, W. et al. Immune cell profiling of COVID-19 patients in the recovery stage by single-cell sequencing. *Cell Discov.* https://doi.org/10.1038/s41421-020-0168-9 (2020).
19. Deng, W. et al. Primary exposure to SARS-CoV-2 protects against reinfection in rhesus macaques. *Science* **369**, 818–823 (2020).

20. de Wit, E. et al. Prophylactic and therapeutic remdesivir (GS-5734) treatment in the rhesus macaque model of MERS-CoV infection. *Proc. Natl Acad. Sci. USA* **117**, 6771–6776 (2020).

21. Caswell, J. L. & Williams K. in *Jubb, Kennedy and Palmer's Pathology of Domestic Animals* 5th edn (eds Maxie M. G. et al.) 523–655 (Elsevier, 2007).

22. Grifoni, A. et al. Targets of T cell responses to SARS-CoV-2 coronavirus in humans with COVID-19 disease and unexposed individuals. *Cell* **181**, 1489–1501 (2020).

23. Letsch, A. & Scheibenbogen, C. Quantification and characterization of specific T-cells by antigen-specific cytokine production using ELISPOT assay or intracellular cytokine staining. *Methods* **31**, 143–149 (2003).

24. Connors, J. M. & Levy, J. H. COVID-19 and its implications for thrombosis and anticoagulation. *Blood* **135**, 2033–2040 (2020).

25. Ranucci, M. et al. The procoagulant pattern of patients with COVID-19 acute respiratory distress syndrome. *J. Thromb. Haemost.* **18**, 1747–1751 (2020).

26. Kakuk, T. J. et al. A human respiratory syncytial virus (RSV) primate model of enhanced pulmonary pathology induced with a formalin-inactivated RSV vaccine but not a recombinant FG subunit vaccine. *J. Infect. Dis.* **167**, 553–561 (1993).

27. Nalca, A., Totura, A., Livingston, V., Frick, O. & Dyer, D. African green monkey model of Middle East respiratory syndrome coronavirus (MERS-CoV) infection. *Int. J. Infect. Dis.* **79**, 99–100 (2019).

28. Durbin, A. P., Elkins, W. R. & Murphy, B. R. African green monkeys provide a useful nonhuman primate model for the study of human parainfluenza virus types-1, -2, and -3 infection. *Vaccine* **18**, 2462–2469 (2000).

29. Prasad, A. N. et al. Resistance of cynomolgus monkeys to nipah and hendra virus disease is associated with cell-mediated and humoral immunity. *J. Infect. Dis.* **221**, S436–S447 (2020).

30. Williamson, B. N. et al. Clinical benefit of remdesivir in rhesus macaques infected with SARS-CoV-2. *Nature* **585**, 273–276 (2020).

31. Vogel, A. A prefusion SARS-CoV-2 spike RNA vaccine is highly immunogenic and prevents lung infection in non-human primates. Preprint at *bioRxiv* https://doi.org/10.1101/2020.09.08.280818 (2020).

32. Grant, M. C. et al. The prevalence of symptoms in 24,410 adults infected by the novel coronavirus (SARS-CoV-2; COVID-19): a systematic review and meta-analysis of 148 studies from 9 countries. *PLoS ONE* https://doi.org/10.1371/journal.pone.0234765 (2020).

33. Tian, S. et al. Pulmonary pathology of early-phase 2019 novel coronavirus (COVID-19) pneumonia in two patients with lung cancer. *J. Thorac. Oncol.* **15**, 700–704 (2020).

34. Ackermann, M. et al. Pulmonary vascular endothelialitis, thrombosis, and angiogenesis in COVID-19. *N. Engl. J. Med.* **383**, 120–128 (2020).

35. Martines, R. B. et al. Pathology and pathogenesis of SARS-CoV-2 associated with fatal coronavirus disease, United States. *Emerg. Infect. Dis.* **26**, 2005–2015 (2020).

36. American College of Radiology. *ACR Recommendations for the use of Chest Radiography and Computed Tomography (CT) for Suspected COVID-19 Infection* https://www.acr.org/Advocacy-and-Economics/ACR-Position-Statements/Recommendations-for-Chest-Radiography-and-CT-for-Suspected-COVID19-Infection (2020).

37. Weinstock, M. E. et al. Chest X-ray findings in 636 ambulatory patients with COVID-19 presenting to an urgent care center: a normal chest X-ray is no guarantee. *J. Urgent Care Med.* **14**, 13–18 (2020).

38. Rubin, G. D. et al. The role of chest imaging in patient management during the COVID-19 pandemic: a multinational consensus statement from the Fleischner Society. *Radiology* **296**, 172–180 (2020).

39. Diao, B. et al. Human kidney is a target for novel severe acute respiratory syndrome coronavirus 2 (SARS-CoV-2) infection. Preprint at *medRxiv* https://doi.org/10.1101/2020.03.04.20031120 (2020).

40. Chen, X. et al. Detectable serum SARS-CoV-2 viral load (RNAaemia) is closely correlated with drastically elevated interleukin 6 (IL-6) level in critically ill COVID-19 patients. *Clin. Infect. Dis.* https://doi.org/10.1093/cid/ciaa449 (2020).

41. Callow, K. A., Parry, H. F., Sergeant, M. & Tyrrell, D. A. J. The time course of the immune response to experimental coronavirus infection of man. *Epidemiol. Infect.* **105**, 435–446 (1990).

42. Galanti, M. & Shaman, J. Direct observation of repeated infections with endemic coronaviruses. *J. Infect. Dis.* https://doi.org/10.1093/infdis/jiaa392 (2020).

Methods

Virus. The virus (SARS-CoV-2/INMI1-Isolate/2020/Italy) employed in this study was isolated on 30 January 2020 from the sputum of the first clinical patient in Italy, a tourist visiting from the Hubei province of China who developed respiratory illness while traveling[43]. The virus was initially passaged twice (P2) on Vero E6 cells; the supernatant and cell lysate were collected and clarified following a freeze/thaw cycle. This isolate is certified as *Mycoplasma*-free. The complete sequence was submitted to GenBank (MT066156) and is available on the GISAID website (BetaCoV/Italy/INMI1-isl/2020: EPI_ISL_410545) upon registration. For in vivo challenge, the P2 virus was propagated on Vero E6 cells and the supernatant was collected and clarified by centrifugation, making the virus used in this study a P3 stock.

Animal challenge. SARS-CoV-2 seronegative AGMs (*Chlorocebus aethiops*) (four females, two males) (St Kitts origin, Worldwide Primates) were randomized into two cohorts where one group ($n = 3$) was scheduled for euthanasia at 5 dpi and the other to be back-challenged ($n = 3$) with the same SARS-CoV-2 isolate and dose. Animals were anesthetized with ketamine and inoculated with a combined 4.6×10^5 p.f.u. dose of SARS-CoV-2 with 2.3×10^5 p.f.u. delivered by the intratracheal route in 5.0 ml and 2.3×10^5 p.f.u. delivered by the intranasal route in 1.0 ml total (0.5 ml per nostril). All subjects were longitudinally monitored for clinical signs of illness, including temperature (measured by surgically implanted DST micro-T small implantable thermo loggers (Star-Oddi)), respiration quality and clinical pathology. All measurements requiring physical manipulation of the animals were performed under sedation by ketamine or telazol. Animal protocols were approved by the University of Texas Medical Branch (UTMB) Institutional Animal Care and Use Committee and adhere to the National Institutes of Health Guide for the Care and Use of Laboratory Animals. Further information on research design is available in the Nature Research Reporting Summary linked to this article.

Radiographic technique. All monkeys were imaged with a portable GE AMX-4+ computed radiography system using a DRTECH detector set at a 36-inch focal film distance. Images were captured and evaluated using the Maven Patient Image Voyance Software (v.2020) in ventral dorsal and right lateral positions at 50 kVp and 12.5 mA as previously described[44]. Chest radiographs were captured and interpreted by a double-board-certified clinical veterinarian and veterinary pathologist and reviewed by a MD-board-certified radiologist.

RNA isolation from SARS-CoV-2-infected AGMs. On specified procedure days (days 0, 2, 3, 4, 5, 7, 12, 15 and 21), 100 μl of blood or BAL fluid was added to 600 μl of AVL viral lysis buffer (QIAGEN) for virus inactivation and RNA extraction. Following removal from the high containment laboratory, RNA was isolated from blood, BAL fluid and mucosal swabs using the QIAamp viral RNA kit (QIAGEN). Tissues were put into RNAlater, inactivated with QIAGEN RLT buffer and extracted using a QIAGEN RNeasy Mini kit.

Detection of SARS-CoV-2 load. vRNA was quantified using the US Centers for Disease Control-designed SARS-CoV-2 N2 assay primers/probe for reverse transcriptase quantitative PCR (RT–qPCR)[45]. SARS-CoV-2 RNA was detected using One-step probe RT–qPCR kits (QIAGEN) and a CFX96 detection system (Bio-Rad) with the following cycle conditions: 50 °C for 10 min, 95 °C for 10 s and 45 cycles of 95 °C for 10 s and 55 °C for 30 s. Threshold cycle (C_T) values representing SARS-CoV-2 genomes were analyzed with CFX Manager Software and the data are presented as GEq. To generate the GEq standard curve, SARS-CoV-2 RNA from cell supernatants was serially diluted and the number of genomes was calculated using Avogadro's number and the molecular weight of the SARS-CoV-2 genome.

Virus titration was performed by plaque assay with Vero E6 cells (ATCC CRL-1586). Briefly, increasing tenfold dilutions of samples were adsorbed to Vero E6 cell monolayers in duplicate wells (200 μl). Cells were overlaid with EMEM agar medium plus 1.25% Avicel, incubated for 2 d and plaques were counted after staining with 1% crystal violet in formalin.

Hematology and serum biochemistry. Total white blood cell counts, white blood cell differentials, red blood cell counts, platelet counts, hematocrit values, total hemoglobin concentrations, mean cell volumes, mean corpuscular volumes and mean corpuscular hemoglobin concentrations were analyzed from blood collected in tubes containing EDTA using a Vetscan HM5 hematologic analyzer (Abaxis). Serum samples were tested for concentrations of albumin, amylase, ALT, aspartate aminotransferase, alkaline phosphatase, blood urea nitrogen, calcium, CRE, CRP, GGT, glucose, total protein and uric acid using a Piccolo point-of-care analyzer and Biochemistry Panel Plus analyzer discs (Abaxis). Partial pressures of CO_2 and O_2 were obtained using an iSTAT Alinity hematological analyzer (Abbott).

ELISA. SARS-CoV-2-specific IgG and IgA antibodies were measured in sera by ELISA at the indicated time points. Immunosorbent 96-well plates were coated overnight with each antigen. To detect spike IgA or IgG, plates were coated with 0.1 μg ml^{-1} spike S1 plus S2 ectodomain (Sino Biologicals; cat. no.

40589-V08B1) or RBD (BEI; cat. no. NR-52366). For total virus-specific IgG, plates were coated with a 1:1,000 dilution of irradiated SARS-CoV-2-infected or normal Vero E6 lysate in PBS (pH 7.4) kindly provided by T.W. Ksiazek (UTMB). Nucleoprotein ELISA kits were kindly provided by Zalgen Labs. Sera were initially diluted 1:100 and then twofold through 1:25,600 in 4% BSA in 1× PBS or in Zalgen-provided reagents. After a 1-h incubation, plates were washed six times with wash buffer (1× PBS with 0.2% Tween-20) and incubated for 1 h with a 1:5,000 or 1:600 dilution of HRP-conjugated anti-primate IgG antibody (Fitzgerald Industries International; cat. no. 43R-IG020HRP) or anti-primate IgA antibody (Rockland Immunochemicals; cat. no. 617-103-006), respectively. RT SigmaFast O-phenylenediamine substrate (P9187, Sigma) was added to the wells after six additional washes to develop the colorimetric reaction. The reaction was stopped with 3 M sulfuric acid 5–10 min after O-phenylenediamine addition and absorbance values were measured at a wavelength of 492 nm on a spectrophotometer (Biotek Cytation5 system). For Zalgen kits, tetramethylbenzidine was used to develop the reaction; the reaction was stopped with methanesulfonic acid and plates were read at a wavelength of 450 nm. Absorbance values were normalized by subtracting uncoated wells from antigen-coated wells at the corresponding serum dilution. End-point titers were defined as the reciprocal of the last adjusted serum dilution with a value ≥0.20.

ELISPOT. To analyze cellular responses, AGM PBMCs were rapidly thawed in a water bath at 37 °C and resuspended in pre-warmed complete RPMI 1640 medium with 10% FBS, 1% GlutaMAX (Thermo Fisher Scientific) and 1% penicillin-streptomycin (Thermo Fisher Scientific). Cells were rested overnight at 37 °C and 5% CO_2 and left unstimulated or stimulated for 24 h at 37 °C and 5% CO_2 with either lectin (Sigma-Aldrich) from *Phytolacca americana* (PWM), one of two PepMix SARS-CoV-2 spike peptide pools (JPT) spanning the length of the protein or a SARS-CoV-2 nucleoprotein peptide pool (BEI). The spike pools contained 158 or 157 15mer peptides with 11 amino acid overlaps and the N pool contained 13mer peptides with 10 amino acid overlaps. S and N pools were prepared in dimethylsulfoxide and used at a final concentration of 1 μg ml^{-1}. Unstimulated cells contained 0.2% dimethylsulfoxide by volume. As a positive control, PBMCs were stimulated with PWM at a final concentration of 2.5 μg ml^{-1}. For ELISPOT analysis, samples were stained using dual color primate IL-2 and IFN-γ kits (R&D Systems) according to the manufacturer's recommendations. PBMCs were plated at 2.5×10^5 cells per well in a 96-well plate coated with nonhuman primate IL-2 and IFN-γ capture antibodies. Following a 24-h incubation at 37 °C and 5% CO_2, ELISpot plates were imaged using an Immunospot S6 UNIVERSAL Analyzer (Cellular Technology Limited). Reported values were calculated by subtracting the number of SFCs in a given unstimulated sample from its respective stimulated counterpart at the corresponding dpi.

Serum neutralization assay. Neutralization titers were calculated by determining the dilution of serum that reduced 50% of plaques (PRNT$_{50}$). We incubated a standard 100 p.f.u. amount of SARS-CoV-2 with twofold serial dilutions of serum samples for 1 h. The virus–serum mixture was then used to inoculate Vero E6 cells for 60 min. Cells were overlaid with EMEM agar medium plus 1.25% Avicel, incubated for 2 d and plaques were counted after staining with 1% crystal violet in formalin. End-point PRNT$_{50}$ titers were defined as the reciprocal of the last serum dilution with an approximate PRNT$_{50}$ value.

Bead-based cytokine and coagulation immunoassays. Concentrations of immune mediators and fibrinogen were determined by flow cytometry using LegendPlex multiplex technology (BioLegend). Serum concentrations of cytokines/chemokines and plasma concentrations of fibrinogen were quantified using Nonhuman Primate Inflammation 13-plex (1:4 dilution) and Human Thrombosis (1:100 dilution) kits or a Human Fibrinolysis (1:10,000 dilution) panel, respectively. Samples were processed in duplicate following the kit instructions and recommendations. Following bead staining and washing, 1,500–4,000 bead events were collected on a FACS Canto II cytometer (BD Biosciences) using BD FACS Diva software. The raw.fcs files were analyzed with BioLegend's cloud-based LEGENDplex Data Analysis software.

RNA sample preparation for transcriptomic analysis. NHPV2_Immunology reporter and capture probesets (Nanostring Technologies) were hybridized with ~5 μl of blood RNA or ~200 ng of BAL RNA at 65 °C for ~24 h. The RNA:probeset complexes were loaded into an nCounter microfluidics cartridge and assayed on a Nanostring nCounter SPRINT Profiler. To estimate abundance of each of the 769 unique mRNA immune-related targets included in the NHPV2_Immunology panel, fluorescent reporter barcodes were imaged and counted in each sample lane. In conjunction with the predefined NHP targets, angiotensin-converting enzyme 2 expression and SARS-CoV-2-specific targets (envelope, membrane, nucleocapsid, orf1ab, orf3a, orf7a, orf8, spike) were analyzed in BAL samples with a Nanostring COVID-19 Plus Panel Plus kit.

Bioinformatics analysis. The nCounter RCC files were imported into Nanostring nSolver 4.0 software. All samples met the established quality control criteria. To compensate for varying RNA inputs, housekeeping genes and spiked-in positive

and negative controls were used to normalize raw counts. The data were analyzed using the Nanostring nSolver Advanced Analysis 2.0 package to generate the principal-component analysis figures and volcano plots, as well as to determine differential expression of transcripts compared to a pre-challenge baseline (a full list of probes detected for each sample group along with fold change values, standard error, confidence limits and *P* values is featured in Supplementary Data). Normalized data (log fold change values and FDR-adjusted *P* values) were exported as a.CSV file (Microsoft Excel Office for Mac v.14.1.0) for ingenuity pathway analysis-based (QIAGEN) functional enrichment of DE RNAs. *Z* scores were imported into GraphPad Prism v.8 to produce canonical signaling, upstream regulator and causal network heat maps. Jak/STAT signaling pathways and IFN-α regulation depictions were also generated with ingenuity pathway analysis. To generate the network maps, DE mRNAs with an FDR-adjusted *P* value <0.05 from each BAL or blood dataset were imported into Metascape and visualized using Cytoscape[46].

Histopathology and immunohistochemistry. Necropsy was performed on all subjects euthanized at 5 dpi. Tissue samples of all major organs were collected for histopathologic and IHC examination and immersion-fixed in 10% neutral buffered formalin for >7 d. Specimens were processed and embedded in paraffin and sectioned at 5-μm thickness. For IHC, specific anti-SARS immunoreactivity was detected using an anti-SARS nucleocapsid protein rabbit primary antibody at a 1:800 dilution for 60 min (Novusbio). The tissue sections were processed for IHC using Lab Vision Autostainer 360 (Thermo Fisher Scientific). Secondary biotinylated goat anti-rabbit IgG (Vector Laboratories) antibody was used at 1:200 dilution for 30 min followed by Vector Streptavidin Alkaline Phosphatase at a dilution of 1:200 for 20 min (Vector Laboratories). Slides were developed with Bio-Red (Biopath) for 7 min and counterstained with hematoxylin for 1 min. For IHC, specific anti-fibrin was detected using an anti-fibrin monoclonal mouse primary antibody at a 1:3,200 dilution for a 60 min incubation (Sekisui Diagnostics). The tissue sections were processed for IHC using Lab Vision Autostainer 360 (Thermo Fisher Scientific). Secondary biotinylated goat anti-mouse IgG (Vector Laboratories) antibody was used at a concentration of 1:200 for 30 min followed by Vector Streptavidin Alkaline Phosphatase at a dilution of 1:200 for 20 min (Vector Laboratories). Slides were developed with Bio-Red (Biopath Laboratories) for 7 min and counterstained with hematoxylin for 1 min.

SARS-CoV-2 RNA in situ hybridization in formalin-fixed paraffin-embedded tissues was performed using an RNAscope 2.5 high definition RED kit (Advanced Cell Diagnostics) according to the manufacturer's instructions. Twenty ZZ probe pairs targeting the genomic SARS-CoV-2 spike protein (S) gene were designed and synthesized by Advanced Cell Diagnostics (cat. no. 848561). After sectioning, deparaffinization with xylene and graded ethanol washes and peroxidase blocking, the sections were heated in RNAscope target retrieval reagent buffer (Advanced Cell Diagnostics cat. no. 322000) for 15 min and air-dried overnight. Sections were digested with Protease III (cat. no. 322340) at 40 °C in a hybridization oven (HybEZ, Advanced Cell Diagnostics cat. no. 321711) for 15 min. Sections were exposed to an in situ hybridization target probe and incubated at 40 °C in a HybEZ oven for 2 h. After rinsing, the signal was amplified using the manufacturer-provided pre-amplifier and the amplifier was conjugated to alkaline phosphatase and incubated with a red substrate-chromogen solution for 10 min, counterstained with hematoxylin, air-dried and cover-slipped. Tissues were stained following package instructions for collagen with the Trichrome One-Step Blue & Red Stain kit (American MasterTech Scientific Laboratory Supplies).

Statistics and reproducibility. Statistical analyses of data were implemented using GraphPad Prism v.8.2.1. The data were fitted to a mixed model, which uses a compound symmetry covariance matrix and is fitted using restricted maximum likelihood, in the absence of missing values. This method gives the same *P* values and multiple comparisons tests as a repeated-measures analysis of variance. Statistics were derived from $n = 6$ individual animal subject samples for all time points before or on 5 dpi and $n = 3$ individual animal subject samples for time points after 5 dpi in a single independent experiment (one cohort was euthanized at 5 dpi ($n = 3$); the other cohort was held to 57/22 dpi ($n = 3$)). Statistics for all figures were calculated from individual animal data values, not technical, replicates. For experiments with technical replicates (for example, duplicate RT–qPCR reactions/wells), only the mean was used to calculate statistical significance. Lung severity scores were analyzed using a two-tailed Student's *t*-test ($P = 0.0249$; $t = 3.500$, d.f. = 4). Tissue PCR and plaque assay titers were analyzed using multiple two-tailed Student's *t*-tests with the Bonferroni–Dunn method. PCR: RLL ($P = 0.0003$ (adjusted); $t = 4.593$, d.f. = 136); RML ($P = 0.0017$; $t = 4.185$, d.f. = 136); RUL ($P = 0.002$; $t = 4.146$, d.f. = 136); LML ($P = 0.0021$; $t = 4.137$, d.f. = 136); LLL ($P = 0.0021$; $t = 4.131$, d.f. = 136); Trac ($P = 0.0025$; $t = 4.085$, d.f. = 136); NaMu ($P = 0.007$; $t = 3.814$, d.f. = 136); Sto ($P = 0.0162$; $t = 3.580$, d.f. = 136). Plaque: RLL ($P = 0.0181$ (adjusted); $t = 3.548$, d.f. = 136); RML ($P = 0.0102$; $t = 3.712$, d.f. = 136); RUL ($P = 0.0007$; $t = 4.405$, d.f. = 136); LML ($P = 0.0037$; $t = 3.983$, d.f. = 136); LLL ($P = 0.0002$; $t = 4.690$, d.f. = 136); LUL ($P < 0.0001$; $t = 4.908$, d.f. = 136). A mixed effects model with Geisser–Greenhouse correction and a Tukey's multi-comparisons test was used to determine statistical significance between individual vRNA probes, revealing no significance between individual probes at each time point, but significant overall time-dependent effects ($P = 0.0003$;

$F_{(1.617, 73.32)} = 10.56$). A multiple hypothesis Benjamini–Hochberg FDR-corrected *P* value <0.05 was deemed significant for all RNA expression analyses, unless otherwise stated. No data points were excluded from our analyses.

Representative photomicrographs were qualitatively considered to display lesions that were nominally or ordinally measured by masking of the pathologist after examination and ranking lesions to satisfy study objectives. Additionally, a thorough examination of multiple slides of target tissues (for example 18 slides of lung) multiple times (up to three times per tissue) was performed in a timely manner to maintain interpretation consistency.

Reporting Summary. Further information on research design is available in the Nature Research Reporting Summary linked to this article.

Data availability
RNA read data and statistics are provided in the Supplementary Data. Other data that support the findings of this study are available from the corresponding author, T.W.G., upon reasonable request.

References
43. Capobianchi, M. R. et al. Molecular characterization of SARS-CoV-2 from the first case of COVID-19 in Italy. *Clin. Microbiol. Infect.* **26**, 954–956 (2020).
44. Geisbert, T. W. et al. Development of an acute and highly pathogenic nonhuman primate model of nipah virus infection. *PLoS ONE* **5**, 10690 (2010).
45. Centers for Disease Control and Prevention. *CDC 2019-nCoV Real-Time RT–PCR Diagnostic Panel* https://www.cdc.gov/coronavirus/2019-ncov/downloads/List-of-Acceptable-Commercial-Primers-Probes.pdf (2020).
46. Zhou, Y. et al. Metascape provides a biologist-oriented resource for the analysis of systems-level datasets. *Nat. Commun.* https://doi.org/10.1038/s41467-019-09234-665 (2019).

Author contributions
C.W., T.W.G. and R.W.C. conceived and designed the study. J.B.G. and T.W.G. performed the SARS-CoV-2 challenge experiments. D.J.D., J.B.G., K.M., T.W.G. and R.W.C. performed animal procedures and clinical observations. K.N.A., C.B.L. and V.B. performed the clinical pathology assays. C.W., S.L.F. and L.M. processed PBMC and BAL samples. V.B. and S.L.F. performed the SARS-CoV-2 infectivity assays. K.N.A. performed the PCR. N.S.D. performed the immunohistochemistry and in situ hybridization. C.W. performed the ELISAs, multiplex assays and bioinformatics analyses. L.M. performed the ELISPOT assays. K.A.F. performed the X-rays and necropsies and performed analysis of the gross pathology, histopathology, immunohistochemistry and in situ hybridization. J.C.H. and K.A.F. analyzed the thoracic radiographs. All authors analyzed the clinical pathology, virology and immunology data. C.W., A.N.P., K.A.F., T.W.G. and R.W.C. wrote the paper. All authors had access to all of the data and approved the final version of the manuscript.

Competing interests
The authors declare no competing interests.

Additional information
Extended data is available for this paper at https://doi.org/10.1038/s41590-020-00835-8.

Supplementary information is available for this paper at https://doi.org/10.1038/s41590-020-00835-8.

Correspondence and requests for materials should be addressed to T.W.G.

Peer review information *Nature Immunology* thanks the anonymous reviewers for their contribution to the peer review of this work.

Reprints and permissions information is available at www.nature.com/reprints.
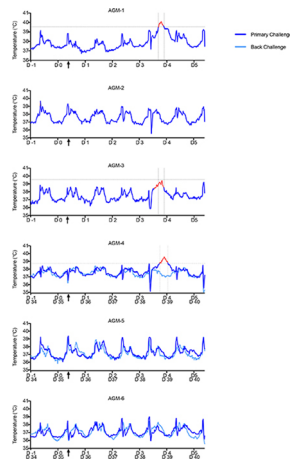
Extended Data Fig. 1 | Longitudinal temperature analysis of AGMs infected with SARS-CoV-2. Prior to challenge, AGMs (n = 6) were surgically implanted with a DST micro-T small implantable thermo logger (Star-Oddi), allowing body temperature measurements for each animal in 15-min increments (96 measurements/day) throughout the course of the study. AGM-1 and AGM-3 had elevated temperatures noticeably above baseline temperatures (1 day prior to challenge) at 3 dpi; AGM-4 exhibited increased temperature at 4 dpi. The 'fever peak' for each subject is colored in red. Vertical dashed lines indicate the start and end of the fever peak. Horizontal dashed lines indicate the threshold temperature for classification as fever. Black arrows on the x-axis indicate time of challenge. Determination of the window of febrile temperatures was performed visually, with comparison of temperatures at all other points during the study duration (-1 dpi to 5 dpi).
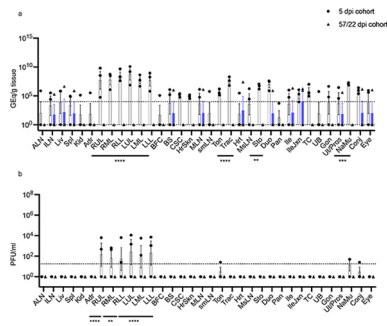
Extended Data Fig. 2 | Comparison of viral loads of tissues from primary and re-challenged AGMs. Tissues harvested at necropsy from SARS-CoV-2 infected-AGMs (n = 6) were processed to determine viral loads by **a**, RT-qPCR and **b**, plaque titration. Tissues from animals euthanized at 5 dpi (n = 3) were compared to those re-challenged at 35 dpi and euthanized at 57/22 dpi (n = 3). Abbreviations for tissues: ALN: Axillary lymph node, ILN: inguinal lymph node, Liv: liver, Spl: spleen, Kid: kidney, Adr: adrenal gland, RUL: right upper lung, RML: right middle lung, RLL: right lower lung, LUL: left upper lung, LML: left middle lung, LLL: left lower lung, BFC: brain frontal cortex, BS: brain stem, CSC: cervical spinal cord, MLN: mandibular lymph node, smLN: submandibular lymph node, Ton: tonsil, Trac: trachea, Hrt: heart, MsLN: mesenteric lymph node, Sto: stomach, Duo: duodenum, Pan: pancreas, Ile: ileum, IleJxn: ileocecal junction, TC: transverse colon, UB: urinary bladder, Gon: gonad, Ut/Pros: uterus/prostate, NaMu: nasal mucosa, Conj: conjunctiva. The horizontal dashed line indicates the LOD for the assay. Multiple two-tailed t-tests using the Bonferroni-Dunn method: p = 0.0332 (*), 0.0021 (**), 0.0002 (***), <0.0001 (****). Data are presented as mean values +/- SEM. Statistics were derived from the mean of duplicate RT-qPCR reactions or wells of each tissue per animal (n = 6 biologically independent animals/samples per tissue in a single experiment; n = 3 animals per cohort (5 or 57/22 dpi).
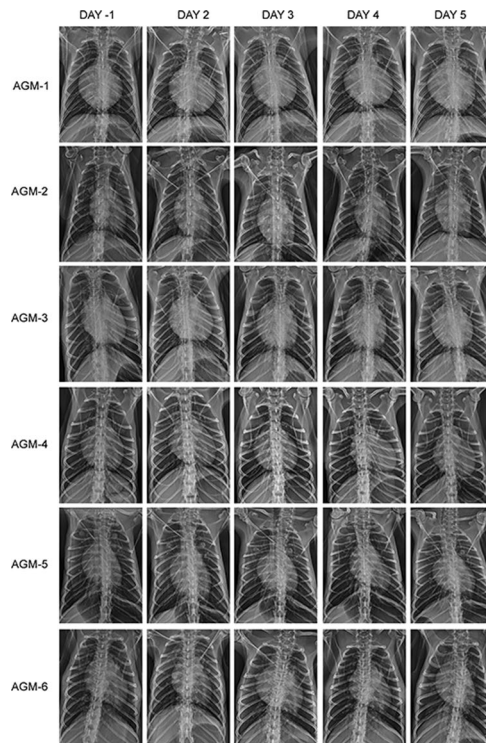
Extended Data Fig. 3 | Temporal radiographs of SARS-CoV-2-infected AGMs. AGMs were imaged with a portable radiography system and detector. Images were captured and evaluated over the course of the study in ventral dorsal (VD) and right lateral (R LAT) positions. Chest radiographs were captured and interpreted by a double board-certified clinical veterinarian and veterinary pathologist and reviewed by a MD board-certified radiologist.
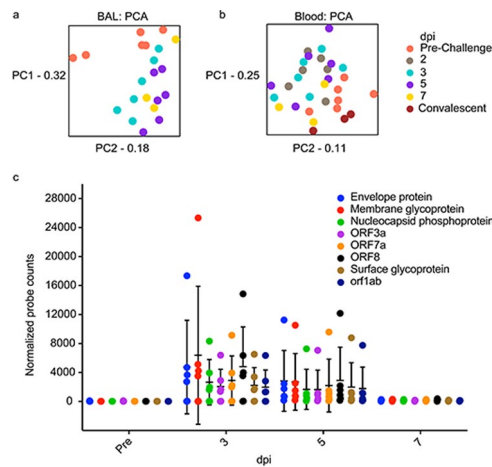
Extended Data Fig. 4 | Analysis of temporal host RNA and virus-specific probe expression in SARS-CoV-2-infected AGM BAL and blood samples.
Principal Component Analyses (PCA) indicate overall sample variance in **a**, BAL and **b**, blood AGM transcriptomes when filtered by day post infection (dpi) and are shown to highlight time-dependent host transcriptional changes. PC1 (principal component 1), PC2 (principal component 2). **c**, At the indicated time point, the expression of individual virus-specific probes in BAL samples of each subject is plotted. Data are presented as mean values +/- SD. Statistics were derived from n=6 biologically independent animals/samples for pre-, 3, and 5 dpi time points and n=3 biologically independent animals/samples for the 7 dpi time point in a single experiment. A mixed effects model with Geisser-Greenhouse correction and a Tukey's multi-comparisons test revealed no statistical significance between individual probes at any particular time point, but significant overall time-dependent effects (p=0.0003).
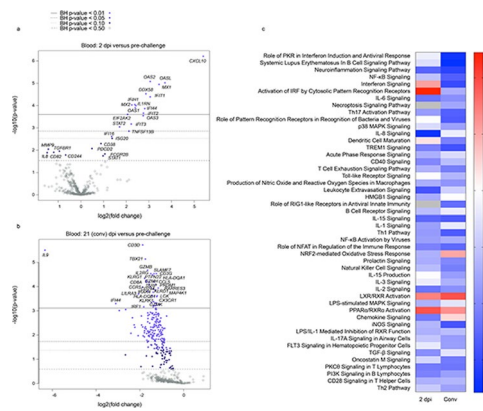
Extended Data Fig. 5 | Early and convalescent stage transcriptional changes in SARS-CoV-2-infected AGMs. a, b, Volcano plots and a **c**, heatmap indicating early and convalescent stage transcriptional changes in SARS-CoV-2-infected AGMs. **a,b**) Displayed are -log10(p-values) and log2 fold changes for each mRNA target. Horizontal lines within the plot indicate FDR-adjusted p-value thresholds. Targets highlighted in blue indicate adjusted p-values < 0.10. A Benjamini-Hochberg test was employed to derive FDR-adjusted p-values. **c**) Heatmap demonstrating the most highly upregulated and downregulated canonical pathways at each time point. Only differentially expressed transcripts with an FDR-corrected p-value of less than 0.1 were enriched with Ingenuity Pathway Analysis (Qiagen). The data were normalized against a day 0 pre-challenge baseline for each NHP subject. Red indicates high expression (z-scores); blue indicates low expression; white indicate similar expression; gray indicates insufficient transcripts mapping to the indicated pathway.
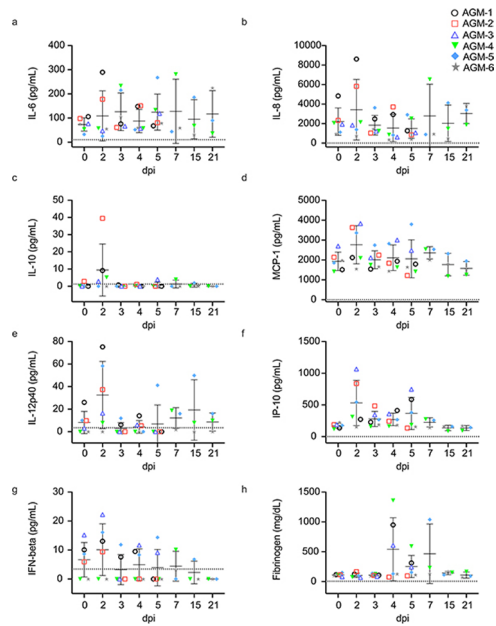
Extended Data Fig. 6 | Soluble inflammatory mediators and coagulation markers detected in SARS-CoV-2 infected AGM sera following primary challenge. a-g, Cytokine and **h**, fibrinogen fold-changes relative to a pre-challenge (0 dpi) baseline in serum or plasma of AGMs infected with SARS-CoV-2 (n = 6 biologically independent animals in a single experiment for 0, 2, 3, 4, and 5 dpi time points; n = 3 for 7, 15, and 21 time points). Data are presented as mean values +/- SD of duplicate samples per subject per analyte in a single experiment.

Corresponding author(s): Thomas W. Geisbert

Last updated by author(s): Oct 27, 2020

Reporting Summary

Nature Research wishes to improve the reproducibility of the work that we publish. This form provides structure for consistency and transparency in reporting. For further information on Nature Research policies, see our Editorial Policies and the Editorial Policy Checklist.

Statistics

For all statistical analyses, confirm that the following items are present in the figure legend, table legend, main text, or Methods section.

n/a	Confirmed	
☐	☒	The exact sample size (*n*) for each experimental group/condition, given as a discrete number and unit of measurement
☐	☒	A statement on whether measurements were taken from distinct samples or whether the same sample was measured repeatedly
☐	☒	The statistical test(s) used AND whether they are one- or two-sided *Only common tests should be described solely by name; describe more complex techniques in the Methods section.*
☐	☒	A description of all covariates tested
☐	☒	A description of any assumptions or corrections, such as tests of normality and adjustment for multiple comparisons
☐	☒	A full description of the statistical parameters including central tendency (e.g. means) or other basic estimates (e.g. regression coefficient) AND variation (e.g. standard deviation) or associated estimates of uncertainty (e.g. confidence intervals)
☐	☒	For null hypothesis testing, the test statistic (e.g. *F*, *t*, *r*) with confidence intervals, effect sizes, degrees of freedom and *P* value noted *Give P values as exact values whenever suitable.*
☒	☐	For Bayesian analysis, information on the choice of priors and Markov chain Monte Carlo settings
☒	☐	For hierarchical and complex designs, identification of the appropriate level for tests and full reporting of outcomes
☒	☐	Estimates of effect sizes (e.g. Cohen's *d*, Pearson's *r*), indicating how they were calculated

Our web collection on statistics for biologists contains articles on many of the points above.

Software and code

Policy information about availability of computer code

Data collection	-RT-qPCR data collection was performed using CFX Maestro 1.1 version 4.1.2433.1219. -Raw Nanostring targeted transcriptome profiling data was exported from the instrument into Nanostring nSolver v4.0 for QC. The data was exported to Microsoft Excel Office 365 v.16.01.13127.20266. -LegendPlex data was collected with a FACS Canto II cytometer (BD Biosciences) using BD FACS Diva software (Version 10.6.1) and LegendPlex cloud-based software (Version 2020.05.14). -Immunospot data was collected using Immunospot Professional v7.0.9.5 -ELISA data was collected using Biotek Cytation5 v.3.04.
Data analysis	-RT-qPCR analysis was performed using CFX Maestro 1.1 version v4.1.2433.1219. -Nanostring data was analyzed using Nanostring nSolver Advanced Analysis 2.0 package to generate principal component analysis (PCA) figures and volcano plots, as well as to determine differential expression of transcripts compared to a pre-challenge baseline. Pathway analysis of this data was performed using Qiagen Ingenuity Pathway Analysis (IPA; Summer Release 2020). Network maps of differentially expressed mRNAs were imported into Metascape 3.5 and visualized using Cytoscape v3.8.0. -LEGENDplex data was analyzed using cloud-based LEGENDplex™ Data Analysis Software. -Immunospot data was analyzed using Immunospot Professional v7.0.9.5 -ELISA data was analyzed by Biotek Cytation5 v.3.04. and Microsoft Excel Office 365 v.16.01.13127.20266. -All statistical analysis was performed in Graphpad Prism v8.2.1.

For manuscripts utilizing custom algorithms or software that are central to the research but not yet described in published literature, software must be made available to editors and reviewers. We strongly encourage code deposition in a community repository (e.g. GitHub). See the Nature Research guidelines for submitting code & software for further information.

Data

Policy information about availability of data

All manuscripts must include a data availability statement. This statement should provide the following information, where applicable:

- Accession codes, unique identifiers, or web links for publicly available datasets
- A list of figures that have associated raw data
- A description of any restrictions on data availability

RNA reads data and statistics are provided as an extended data file (Source Data File 1). Other data that support the findings of this study are available from the corresponding author, T.W.G., upon reasonable request

Field-specific reporting

Please select the one below that is the best fit for your research. If you are not sure, read the appropriate sections before making your selection.

☒ Life sciences   ☐ Behavioural & social sciences   ☐ Ecological, evolutionary & environmental sciences

For a reference copy of the document with all sections, see nature.com/documents/nr-reporting-summary-flat.pdf

Life sciences study design

All studies must disclose on these points even when the disclosure is negative.

Sample size	As SARS-CoV-2 is a novel pathogen in humans, and prior studies in African green monkeys did not exist, animal group size was decided by the expected lethality (low to none, based the limited number of other COVID-19 studies in other species of non-human primates), and for ethical reasons, the minimum number of animals by which statistical inferences could be made (n=6 for antemortem data collected up to 5 dpi, n=3 for postmortem data collected 5 dpi, n=3 for ante- and postmortem data collected beyond 5 dpi).
Data exclusions	No data was excluded from the analysis.
Replication	Due to the ethical and technical challenges experiments involving animals, and specifically non-human primates in high-containment conditions, it was not feasible to conduct multiple experimental repetitions for this study. Representative photomicrographs were qualitatively considered to display lesions that were nominally or ordinally measured by masking of the pathologist post-examination and ranking lesions to satiate the study objectives. Additionally, a thorough examination of multiple slides of the target tissues (e.g. 18 slides of lung) multiple times (up to 3 times per tissue) was performed in a timely manner to maintain interpretation consistency. Other data was collected from a single independent experiment with successful technical replication.
Randomization	Animals were issued a number from 1-6, and randomly assigned to groups using a random number generator.
Blinding	Blinding was not performed for this study, as it was not necessary to answer the questions set forth by the study.

Reporting for specific materials, systems and methods

We require information from authors about some types of materials, experimental systems and methods used in many studies. Here, indicate whether each material, system or method listed is relevant to your study. If you are not sure if a list item applies to your research, read the appropriate section before selecting a response.

Materials & experimental systems

n/a	Involved in the study
☐	☒ Antibodies
☐	☒ Eukaryotic cell lines
☒	☐ Palaeontology and archaeology
☐	☒ Animals and other organisms
☒	☐ Human research participants
☒	☐ Clinical data
☒	☐ Dual use research of concern

Methods

n/a	Involved in the study
☒	☐ ChIP-seq
☒	☐ Flow cytometry
☒	☐ MRI-based neuroimaging

Antibodies

Antibodies used	-Goat anti-Monkey IgG HRP pAb (Fitzgerald, Cat# 43R-IGO20-HRP, Lot# c15032720) -Monkey IgA alpha Antibody Peroxidase Conjugated (Rockland Immunochemicals, Cat # Cat: 617-103-006, Lot # 41791) -SARS Nucleocapsid Protein Antibody (Novus Biologicals, Cat # NB100-56683, Lot # 111003D-4) -Goat Anti-Rabbit IgG Antibody (H+L), Biotinylated (Vector Laboratories, Cat # BA-1000, Lot # ZG0122)

	-Anti-fibrin monoclonal mouse primary antibody (Sekisui Diagnostics, Cat # REF 350, Lot# 140714) -Goat Anti-Mouse IgG Antibody (H+L), Biotinylated (Vector Laboratories, Cat # BA-9200, Lot # ZB0324)
Validation	-Goat anti-Monkey IgG HRP pAb- The antibody has been validated by Western blot by the manufacturer. Data within this manuscript and PMID 32719371 validates its use for ELISA. -Monkey IgA alpha Antibody Peroxidase Conjugated- The antibody has been validated for ELISA by the manufacturer. -SARS Nucleocapsid Protein Antibody- The antibody has been validated for IHC-detection of SARS-CoV-2 nucleocapsid protein by the manufacturer and in this publication. Orthogonal strategies validation by vendor (Novus Biologicals): Dual RNAscope ISH-IHC: SARS Nucleocapsid Protein Antibody [NB100-56683] - Formalin-fixed paraffin-embedded tissue sections of SARS-CoV-2 infected human lung tissue were probed for SARS-CoV-2 viral RNA (ACD anti-sense specific probe v-nCoV2019-S [848561]); Fast Red chromogen, ACD [322360]). Adjacent tissue section was processed for immunohistochemistry using rabbit polyclonal anti-SARS Nucleocapsid Antibody [NB100-56683] at 15ug/mL with 1 hr incubation at 25 degrees Celsius followed by incubation with anti-rabbit IgG VisUCyte HRP Polymer Antibody [VC003] and DAB chromogen (yellow-brown). Tissue was counterstained with hematoxylin (blue). Specific staining was localized to SARS-CoV-2 infected cells. - Goat Anti-Rabbit IgG Antibody (H+L), Biotinylated- The antibody has been validated for IHC by the manufacturer. -Anti-fibrin monoclonal mouse primary antibody- The antibody has been validated for IHC by the manufacturer. This exact antibody is now offered by Biomedica Diagnostics (ref 350). For validation, this antibody was shown to successfully stain fibrin (beta chain of fibrinogen) in snap frozen human cardiac allografts. The antibody also successfully stained fibrin in formalin-fixed, paraffin embedded canine mammary neoplastic tissue and in formalin-fixed paraffin embedded rabbit pleural tissue (PMID: 1456881). -Goat Anti-Mouse IgG Antibody (H+L), Biotinylated- The antibody has been validated for IHC by the manufacturer.

Eukaryotic cell lines

Policy information about cell lines

Cell line source(s)	Vero E6 (ATCC CRL-1586) was obtained from American Type Culture Collection (ATCC).
Authentication	Independent validation of the Vero E6 cell line was not performed outside of any authentication performed by ATCC.
Mycoplasma contamination	Cells were tested for mycoplasma contamination. No detectable mycoplasma or endotoxin levels were measured (< 0.5 endotoxin units (EU)/ml).
Commonly misidentified lines (See ICLAC register)	No commonly misidentified cell lines were used in the study.

Animals and other organisms

Policy information about studies involving animals; ARRIVE guidelines recommended for reporting animal research

Laboratory animals	Research-naive adult African green monkeys (Chlorocebus aethiops); 4 females, 2 males. The age of laboratory animals used in this study was not provided by the vendor.
Wild animals	No wild animals were used in the study.
Field-collected samples	No field-collected samples were used in the study.
Ethics oversight	The animal studies were performed at the Galveston National Laboratory, University of Texas Medical Branch at Galveston (UTMB) and were approved by the UTMB Institutional Animal Care and Use Committee. This facility is fully accredited by the Association for Assessment and Accreditation of Laboratory Animal Care International.

Note that full information on the approval of the study protocol must also be provided in the manuscript.